

# UC San Diego

## UC San Diego Electronic Theses and Dissertations

### Title

Experimental Biomechanics of Musculoskeletal Injury Models and Repair Implants

### Permalink

<https://escholarship.org/uc/item/5f27h4cp>

### Author

Caffrey, Jason Patrick

### Publication Date

2020

Peer reviewed|Thesis/dissertation

UNIVERSITY OF CALIFORNIA SAN DIEGO

EXPERIMENTAL BIOMECHANICS OF MUSCULOSKELETAL  
INJURY MODELS AND REPAIR IMPLANTS

A dissertation submitted in partial satisfaction of the  
requirements for the degree Doctor of Philosophy

in

Bioengineering

by

Jason P. Caffrey

Committee in Charge:

Professor Robert L. Sah, Chair  
Professor Shengqiang Cai  
Professor Francisco Contijoch  
Professor Koichi Masuda  
Professor Jeffrey H. Omens

2020

Copyright

Jason P. Caffrey, 2020

All rights reserved.

The Dissertation of Jason P. Caffrey is approved, and it is acceptable in quality and form for publication on microfilm and electronically:

---

---

---

---

---

Chair

University of California San Diego  
2020

# TABLE OF CONTENTS

<b>Signature Page</b> .....	<b>iii</b>
<b>Table of Contents</b> .....	<b>iv</b>
<b>List of Figures</b> .....	<b>viii</b>
<b>List of Tables</b> .....	<b>ix</b>
<b>Acknowledgments</b> .....	<b>x</b>
<b>Vita</b> .....	<b>xii</b>
<b>Abstract of the Dissertation</b> .....	<b>xiv</b>
<b>Chapter 1: Introduction</b> .....	<b>1</b>
1.1 General Introduction to the Dissertation.....	1
1.2 Articular Cartilage and Osteoarthritis.....	4
1.3 Post-Traumatic Osteoarthritis .....	6
1.4 Rabbit ACLT Model.....	8
1.5 Mechanics and Mechanobiology of Orthopaedic Devices .....	9

1.6 Degenerative Disc Disease and Spinal Fusion Implants..... 10

1.7 References..... 11

**Chapter 2: Joint-scale Mechano-pathology in Post-Traumatic Osteoarthritis: Ex Vivo Imposed Gait-like Loading of ACL-transected Rabbit Knees Induces Abnormal Kinematics and Cartilage Degeneration .....15**

2.1 Abstract..... 15

2.2 Introduction..... 18

2.3 Methods..... 21

2.4 Results..... 31

2.5 Discussion..... 39

2.6 Acknowledgments..... 42

2.7 References..... 43

**Chapter 3: Ex Vivo Loading of Trussed Implants for Spine Fusion Induces Heterogeneous Strains Consistent with Homeostatic Bone Mechanobiology .....46**

3.1 Abstract..... 46

3.2 Introduction..... 48

3.3 Methods.....	51
3.4 Results.....	60
3.5 Discussion.....	73
3.6 Acknowledgments.....	75
3.7 References.....	76
<b>Chapter 4: Strains in Trussed Spine Interbody Fusion Implants are Modulated by Load and Design .....</b>	<b>80</b>
4.1 Abstract.....	80
4.2 Introduction.....	82
4.3 Materials and Methods.....	84
4.4 Results.....	91
4.5 Discussion.....	98
4.6 Acknowledgments.....	102
4.7 References.....	103

<b>Chapter 5: Conclusions .....</b>	<b>106</b>
5.1 Summary of Findings.....	106
5.2 Discussion.....	109
5.3 References.....	113



## LIST OF FIGURES

Figure 2.1: Study design. ....	26
Figure 2.2: Mechanical loading setup. ....	27
Figure 2.3: Laxity testing. ....	33
Figure 2.4: Regional India ink reflectance scores. ....	36
Figure 2.5: Areas of cartilage surface degeneration by HiReD-IIIS. ....	37
Figure 2.6: Multi-scale imaging of cartilage degeneration. ....	38
Figure 3.1: Structure of 4WEB ALIF cage with affixed fiducial sphere markers. ....	56
Figure 3.2: Cage loading configuration. ....	57
Figure 3.3: Intra-cage strain distribution for repeated loading by vertebral platens. ....	62
Figure 3.4: Intra-cage strain distribution for controls. ....	67
Figure 3.5: Inter-cage strain distribution for loading by vertebral platens. ....	69
Figure 3.6: Intra-cage strain distribution for repeated loading by plastic platens. ....	72
Figure 4.1: Design of trussed cages with affixed fiducial markers. ....	88
Figure 4.2: Strain distribution for 0.75mm cages. ....	92
Figure 4.3: Strain distribution for 1.00mm cages. ....	94

## LIST OF TABLES

Table 2.1: Cartilage grading system. ....	30
Table 3.1: Study groups for each aim for unloaded and loaded cages. ....	53
Table 3.2: Deformation and strain of all struts. ....	63
Table 3.3: Deformation and strain of vertical struts. ....	64
Table 3.4: Amplitudes of deformation and strain of all struts. ....	66
Table 4.1: Study groups for 1.00mm and 0.75mm cages loaded at 50N, 1000N, or 2000N.....	86
Table 4.2: Deformation and strain of all struts. ....	93
Table 4.3: Deformation and strain of vertical struts. ....	95
Table 4.4: Amplitudes of deformation and strain of all struts. ....	97

## ACKNOWLEDGMENTS

I would first like to greatly acknowledge my graduate research advisor and dissertation committee Chair, Dr. Robert L Sah. Thank you for the many opportunities to learn and for always challenging me to drive my curiosity and enhance my knowledge. I will always be grateful for the countless hours you have spent working on projects, papers, presentations, and proposals in our mission to push the boundaries of knowledge and technology. You have guided me through a journey of personal development and learning over the past ten years.

I would also like to thank the other members of my dissertation committee: Dr. Shengqiang Cai, Dr. Francisco Contijoch, Dr. Koichi Masuda, and Dr. Jeffrey H. Omens for their valuable questions, feedback, and suggestions. I would especially like to thank Dr. Masuda for always supporting and assisting with my research endeavors.

I would like to thank the many members of the CTE lab who have helped me in countless ways over the years. Dr. Bradley Hansen, thank you for being my first lab mentor and pushing me to succeed in my endeavors. Dr. Albert Chen, thank you for the immeasurable help with biomechanical tests and designs. Esther Cory, thank you for all your help with micro-CT imaging. Dr. Michele Temple-Wong, thank you for your input and support over the years. Van Wong, thank you for continually helping me navigate the lab, as well with technical support for my projects. I would also like to thank Susanna Lin, Dr. Felix Hsu, Dr. Neil Chang, Dr. Yang Sun, and Dr. Aimee Raleigh, and Dr. Somaye Jafari for our many discussions and collaborations. To Erica Gacasan, Rebecca Drake, Nasim Eshragh Nia, and Alborz Jelvani, thank you for your support and friendship. I wish you the best of success with your graduate studies and beyond. I consider all of you to be my friends and I will always cherish our times together. Finally, I am

immensely grateful for the support of my amazing wife Eileen, parents, brother, and friends during my time at UC San Diego. Thank you for your patience and encouragement.

Chapter 2 has been submitted to *The American Journal of Sports Medicine*. The dissertation author was the primary author and thanks co-authors Nasim Eshragh Nia, Alborz Jelvani, Erica G. Gacasan, Aileen Liao, Blair T. Caccam, Albert C. Chen, Koichi Masuda, Robert L. Sah. This work was supported by National Science Foundation Graduate Research Fellowship under Grant No DGE-1144086 (JPC), DOD grant OR13085, and Jack Kent Cooke Graduate Fellowships (NEN, AJ).

Chapter 3 was published in *Journal of Biomechanics*. The dissertation author was the primary author and thanks co-authors Esther Cory, Van W. Wong, Koichi Masuda, Albert C. Chen, Jesse P. Hunt, Timothy M. Ganey, and Robert L. Sah. This work was supported by 4WEB Medical (RLS) and the National Science Foundation Graduate Research Fellowship under Grant No DGE-1144086 (JPC).

Chapter 4 was published in *Journal of the Mechanical Behavior of Biomedical Materials*. The dissertation author was the primary author and thanks co-authors Eloy Alonso, Koichi Masuda, Jesse P. Hunt, Cameron N. Carmody, Timothy M. Ganey, and Robert L. Sah. This work was supported by 4WEB Medical (RLS) and the National Science Foundation Graduate Research Fellowship under Grant No DGE-1144086 (JPC).

I would also like to acknowledge support by the National Institute of Health, without which my studies would not have been possible.

## VITA

- 2011 B.S., Bioengineering: Pre-Medical  
University of California San Diego, La Jolla, California
- 2011-2020 Graduate Student Researcher  
Cartilage Tissue Engineering Laboratory  
University of California San Diego, La Jolla, California
- 2013 M.S., Bioengineering  
University of California San Diego, La Jolla, California
- 2020 Ph.D., Bioengineering  
University of California San Diego, La Jolla, California
- 2021 M.D., School of Medicine  
University of California San Diego, La Jolla, California

### Book Chapter

Caffrey JP, Sah RL. Biomechanics of Musculoskeletal Tissues, in *Orthopaedic Basic Science: Foundations of Clinical Practice*, 4th Ed. R O’Keefe, JJ Jacobs, CR Chu, TA Einhorn, 2013:55-68.

### Journal Articles

Caffrey JP, Eshragh Nia N, Jelvani A, Gacasan EG, Liao A, Caccam BT, Chen AC, Masuda K, Sah RL. Joint-scale mechano-pathology in post-traumatic osteoarthritis: ex vivo imposed gait-like loading of ACL-transected rabbit knees induces abnormal kinematics and cartilage degeneration. *Am J Sports Med*, submitted.

Caffrey JP, Jeffords M, Farnsworth CL, Bomar JD, Upasani VV. Comparison of three pediatric pelvic osteotomies for developmental dysplasia of the hip using patient specific 3-D printed models. *J Pediatr Orthop* 2019;39:e159-164.

Caffrey JP, Alonso E, Masuda K, Hunt JP, Carmody CN, Ganey TM, Sah RL. Strains in trussed spine interbody fusion implants are modulated by load and design. *J Mech Behav Biomed Mater* 2018;80:203-8.

Sun Y, Jiang Y, Cory E, Caffrey JP, Hsu FH, Chen AC, Wang J, Sah RL, Bugbee WD. Pulsed lavage cleansing of osteochondral grafts depends on lavage duration, flow intensity, and graft storage condition. *PLoS One* 2017;12:e0176934.

Cherkasskiy L, Caffrey JP, Szewczyk AF, Cory E, Bomar JD, Farnsworth C, Jeffords M, Wenger DR, Sah RL, Upasani VV. Patient-specific 3D models aid planning for triplane proximal femoral osteotomy in slipped capital femoral epiphysis. *J Child Orthop* 2017;11:147-53.

Caffrey JP, Cory E, Wong VW, Masuda K, Chen AC, Hunt JP, Ganey TM, Sah RL. Ex vivo loading of spine fusion implants induces heterogeneous strains consistent with homeostatic bone mechanobiology. *J Biomech* 2016;49:4090-7.

Roberts TP, Paulson DN, Hirschkoff G, Pratt K, Mascarenas A, Miller P, Han M, Caffrey J, Kincade C, Power W, Murray RE, Chow V, Fisk C, Ku M, Chudnovskaya D, Dell J, Golembki R, Lam P, Blaskey L, Kuschner E, Bloy L, Gaetz WC and Edgar J. Artemis 123: Development of a whole-head infant MEG system. *Front Hum Neurosci* 2014;8:99.

Caffrey JP, Kushnaryov AM, Reuther MS, Wong VW, Briggs KK, Masuda K, Sah RL, Watson D. Flexural properties of native and tissue engineered human septal cartilage. *Otolaryngol Head Neck Surg* 2013;148:576-81.

### Selected Abstracts

Caffrey JP, Nia NE, Jelvani A, Gacasan EG, Walsh KC, Hughey VS, Caccam BT, Liao A, Alvarado-Herrera EG, Mir NA, Chakraborty M, Drake RL, Wong VW, Chen AC, Masuda K, Sah RL. Joint-scale mechano-pathology in post-traumatic osteoarthritis: ex vivo imposed gait-like loading of ACL-transected rabbit knees induces abnormal kinematics and cartilage degeneration. *OARSI 2020 World Congress*, 28:549, 2020.

Caffrey JP, Jeffords M, Farnsworth C, Bomar JD, Upasani VV. Comparison of Three Pediatric Pelvic Osteotomies for Developmental Dysplasia of the Hip Using Patient Specific 3-D Printed Models. *Amer Acad Orthop Surg*, 713, 2019.

Caffrey JP, Jeffords M, Farnsworth C, Upasani VV. Comparison of the Acetabular Osteotomies for Developmental Dysplasia of the Hip Using Patient Specific 3-D Printed Pelvic Models. *Proc Ped Orthop Soc North Am*, 3, 2018.

Caffrey JP, Alonso E, Cory E, Wong VW, Masuda K, Chen AC, Ganey TM, Sah RL. Strains in trussed spine interbody fusion implants are modulated by load and design. *Int Soc Adv Spine Surg* 16:626, 2016.

Caffrey JP, Alonso E, Cory E, Wong VW, Masuda K, Chen AC, Ganey TM, Sah RL. Strains in trussed spine interbody fusion implants are modulated by load and design. *Trans Orthop Res Soc* 41:1770, 2016.

Caffrey JP, Cory E, Wong VW, Masuda K, Chen AC, Sah RL, Ganey TM. Ex vivo loading of spine fusion implants induces heterogeneous strains consistent with homeostatic bone mechanobiology. *Int Soc Adv Spine Surg* 15:276, 2015.

Caffrey JP, Hansen BC, Shia KL, Arnold DP, Samy KE, Chen AC, Cory E, Varghese S, Masuda K, Bugbee WD, Sah RL. Customized osteochondral grafts for cartilage resurfacing: Effects of contour and placement on biomechanics of femoro-tibial contact in the goat. *Trans Orthop Res Soc* 40:351, 2015.

Caffrey JP, Cory E, Wong VW, Masuda K, Chen AC, Ganey TM, Sah RL. Ex vivo loading of a spine fusion implant induces strains consistent with mechanobiological maintenance of bone homeostasis. *Trans Orthop Res Soc* 39:716, 2014.

# **ABSTRACT OF THE DISSERTATION**

EXPERIMENTAL BIOMECHANICS OF MUSCULOSKELETAL INJURY MODELS AND  
REPAIR IMPLANTS

by

Jason P. Caffrey

Doctor of Philosophy in Bioengineering

University of California San Diego, 2020

Professor Robert L. Sah, Chair

Musculoskeletal tissues in the body exhibit unique biomechanical properties which enable tasks including load carrying capacity and movement, which can deteriorate in degenerative disease states and result in structural failure and subsequently loss of function. The study of the biomechanical contributions in injury models and repair implants may elucidate failure mechanisms and predict repair success, respectively. We hypothesize that (1)

mechanically-driven knee injury models can replicate *in vivo* disease patterns in post-traumatic osteoarthritis (PTOA) in the rabbit and (2) reparative spine fusion implants for degenerative disc disease can be modulated to exhibit mechanical properties consistent with mechanobiological bone healing. This dissertation aimed to develop experimental biomechanical approaches for (1) inducing rabbit knee articular cartilage degeneration through *ex vivo* mechanical loading, and (2) assessing and comparing mechanical behavior of spine fusion cage designs.

A novel *ex vivo* approach was developed for rabbit knee articulation to rapidly induce cartilage damage, extending past *in vivo* rabbit studies of PTOA after anterior cruciate ligament transection (ACLT). In this *ex vivo* ACLT mechanical loading model, cycle-dependent cartilage degeneration was higher compared with sham surgery and non-loading controls, as assessed by gross and histological degeneration. These gross degenerative changes resembled changes observed *in vivo* at 4 weeks post-ACLT. This new *ex vivo* rabbit knee loading approach provides a platform to study mechanisms of joint-scale cartilage damage as well as possible interventions.

A novel *ex vivo* biomechanical approach for assessing loaded spinal fusion cages was developed, enabling high spatial resolution strain measures throughout an implant volume. These experimental studies extend past *in vivo* and numerical modeling studies, which are inherently limited by resolution and complexity of loading conditions. Using 3-D imaging to track affixed fiducial markers throughout a trussed spine implant under varying loads, truss-specific strains were quantified, with amplitudes consistent with bone mechanobiological homeostasis. The effect of cage design on truss strains was further studied, which demonstrated that varying design can be used to modulate strain amplitudes. These findings suggest that spine implant designs can be targeted to mechanobiological strain regimes for improved implant bone ingrowth and subsequent fusion success.



# CHAPTER 1

## INTRODUCTION

### 1.1 General Introduction to the Dissertation

Musculoskeletal tissues are reliant on biomechanical properties for proper function in the body. High load-bearing tissues, such as articular cartilage in synovial joints and intervertebral discs in the spine, are prone to mechanical failure with disease. Understanding such tissue failure and subsequent repair strategies necessitate biomechanical studies for both characterization and disease modeling. Simulation and *in vivo* disease course studies have provided insight, but have inherent limitations. Experimental biomechanical approaches offer advantages for modeling and assessing musculoskeletal tissues and repair implants.

The overall motivation of this dissertation was to utilize experimental biomechanical approaches to (a) develop a rabbit ACLT mechanical injury model and (b) assess spine fusion repair implants designs. The objectives of these studies were (1) design and demonstrate an *ex vivo* rabbit knee cyclic articulation loading platform to demonstrate cartilage degeneration (Chapter 2), and (2) design and demonstrate an *ex vivo* spine fusion implant loading system to mechanically characterize implant truss struts for mechanobiologically-relevant strain distributions (Chapters 3,4).

Chapter 1 starts with an introduction to osteoarthritis, particularly focusing on post-traumatic osteoarthritis and mechanical hypotheses for cartilage degeneration. The rabbit ACLT

model for post-traumatic osteoarthritis is reviewed. Principles of biomechanics and mechanobiology are described for orthopaedic implants. Lastly, spine fusion implants and associated mechanical designs are outlined.

Chapter 2, which has been submitted to *The American Journal of Sports Medicine*, develops an *ex vivo* rabbit knee articulation system to mechanically induce cartilage wear through cyclic loading. The effect of ACLT on knee stability is shown through increased anterior-posterior tibial translation during laxity testing and knee articulation. The *ex vivo* mechanical loading approach demonstrates similar degeneration in ACLT rabbit knees, compared with *in vivo* 4 weeks post-ACLT knees. This suggests that abnormal loading in the absence of *in vivo* biological joint changes may serve as a driving force for early degeneration in PTOA.

Chapter 3, which has been published in *Journal of Biomechanics*, combines mechanical loading and high-resolution 3-D imaging to characterize the mechanical behavior of trussed spine fusion implants under load. By tracking affixed markers throughout the implant volume, deformation and strain are computed for individual struts in the loaded implant. The resultant distribution of strut strain amplitudes is consistent with mechanobiological bone homeostasis.

Chapter 4, which has been published in *Journal of the Mechanical Behavior of Biomedical Materials*, utilizes the methodology developed in Chapter 3 to study the effect of implant design and load amplitudes on loaded strut strains. Implants with varying strut diameters are compared and demonstrate that thinner struts result in higher percentages of struts in homeostasis and formation ranges under moderate (1000N) and strenuous (2000N) axial compressive loads. The findings suggest that future cage designs may be modulated to target desired mechanical strain regimes at physiological loads.

Chapter 5 summarizes the major findings of the studies presented here, and discusses the implications for research and understanding of post-traumatic osteoarthritis and orthopedic device mechanics and design.

## 1.2 Articular Cartilage and Osteoarthritis

Articular cartilage (AC) is the load-bearing tissue at the ends of long bones within synovial joints [1, 2]. In the normal state, AC has a unique tissue composition and architecture that enables painless joint articulation under load [2]. This structural tissue integrity is derived from a dense extracellular matrix (ECM) with specialized cells (chondrocytes) interspersed [3]. ECM is composed primarily of water, collagen, and proteoglycans, which enable resistance to high compressive loads. AC is stratified into three main zones by depth: superficial, middle (transitional), and deep (radial). Each zone corresponds with varying tissue composition and architecture. The superficial zone has collagen fibers oriented tangentially to resist shear and tensile loads, whereas the deep zone has collagen fibers oriented perpendicular to the surface to resist compressive loads [3]. Degeneration of AC can lead to pain and loss of joint mobility, particularly in high load-bearing joints such as the knee and hip. As an avascular tissue in the adult, AC has a limited ability to heal and is susceptible to progressive damage, such as with osteoarthritis.

Osteoarthritis (OA) is the most common joint disease and leading cause of disability worldwide [4, 5]. The etiology of OA is complex and multifactorial, involving genetic, biological, and biomechanical components [6]. Advancing age or injury can lead to failure of the AC matrix, and thus mechanical integrity, resulting in cartilage degeneration and erosion. There are many biomechanical contributors to development of OA, including anatomical joint alignment, body mass index, and joint destabilization after injury to synovial structures such as ligaments. In OA, there are notable disturbances in the metabolic regulation of matrix turnover [7]. Notably, inflammatory cytokines interleukin (IL)-1 and tumor necrosis factor (TNF)- $\alpha$

increase synthesis of matrix metalloproteins (MMPs), which decrease matrix synthesis. Anabolic cytokines including insulin-like growth factor I (IGF-I), transforming growth factor (TGF)- $\beta$ , and fibroblast growth factors (FGFs) stimulate matrix synthesis. The balance of such catabolic and anabolic states is altered in OA cartilage. However, the interaction between mechanical and biological contributors to OA remains unclear. Additionally, accelerated development of OA following joint injury is common, known as post-traumatic osteoarthritis.

### **1.3 Post-Traumatic Osteoarthritis**

Post-traumatic osteoarthritis (PTOA) contributes up to 12% of arthritis cases, generally affecting younger, more active patients [8, 9]. The classic example of PTOA is tearing of the anterior cruciate ligament (ACL), which results in immediate destabilization of the knee. About 50% of ACL injured knees will progress to OA within 5-15 after injury [8]. ACL reconstruction following ACL tear has shown improvements in function, but has not shown a reduction in PTOA at 14 years follow-up [10]. Whereas older patients with OA may be effectively treated with joint replacement, this approach is not ideal for the younger population that develops PTOA [11].

The primary mechanical function of the ACL is to restrict anterior translation of the tibia relative to the femur [12]. Thus, ACL tear results in increased anterior translation of the tibia [13]. Clinically, this is assessed by the anterior drawer or Lachman tests as part of a physical exam, in which the tibia is manipulated relative to femur to semi-quantitatively assess the displacement of the tibia [14]. This anterior translation is commonly known as anterior knee laxity. The ACL additionally contributes to the rotational stability of the tibia as a secondary function.

The pathophysiology of accelerated cartilage degeneration in post-traumatic osteoarthritis (PTOA) is unclear, and likely involves changes in both mechanical and biological factors [15-18]. Immediately after injury, joint biomechanics are altered with loss of the ACL [16]. Reconstruction of the ACL after injury is shown to improve knee kinematics, but does not fully restore knee laxity to normal [19]. Additionally, other knee structures are often injured during the acute trauma, including underlying bone, cartilage, and soft tissues such as the menisci [16]. Magnetic resonance imaging (MRI) studies have demonstrated chondral injuries at time of ACL

injury, with subsequent longitudinal (5-7 years) chondral degradation [20]. The initial acute trauma may also induce chondrocyte death/apoptosis and alter cell metabolism, as demonstrated *in vitro* [16].

Inflammatory alterations in the synovial tissues have been hypothesized to contribute to cartilage degeneration following ACL tear [15, 21]. ACL injury often results in hemarthrosis, or bleeding into the synovial fluid, and in release of inflammatory cytokines including IL-1, IL-6, IL-8, TNF- $\alpha$ , as well as MMPs [22, 23]. These metabolic responses may be further activated through mechanobiological processes by altered joint biomechanics, resulting in matrix degradation [24]. The lubricating properties of synovial fluid have also been shown to be disrupted up to 1 year after injury, resulting in higher friction and resultant shear loads during knee articulation [25]. The clinical time course of degeneration due to biomechanical and biological insults remains unclear, making the testing of mechanistic pathways difficult to study in humans.

## 1.4 Rabbit ACLT Model

Many animal models for PTOA in the knee have been studied, most notably the New Zealand White rabbit ACL transection (ACLT) model, in which the ACL is surgically or mechanically divided or ruptured. Early PTOA progression studies in large animal models included sheep, dogs, and cats [26]. Smaller animal mouse models have been developed most prominently for genetic manipulation to study PTOA disease mechanisms [26]. Rabbit models exhibit a joint size amenable to study of tissue and joint mechanics and histology without costs associated with larger animal models. *In vivo* rabbit studies have demonstrated accelerated gross and histologic degeneration of the knee cartilage at 4 and 8 weeks post-ACLT [27, 28]. Alterations of knee stability and mechanical properties of cartilage after ACLT have also been demonstrated [28, 29]. *Ex vivo* micro-CT and MRI studies have described 3-D structural changes in cartilage and underlying osseous tissues at 2, 4, and 8 weeks post-ACLT [30-32]. Recently, ACLT has demonstrated alterations in composition, structure, and biomechanics of articular cartilage at both 2 weeks and 4 weeks after rabbit ACLT [33, 34].

Mechanical overloading due to altered joint biomechanics has been suggested as a driving factor for alterations in cartilage material properties in an *in vivo* overload model [35]. Although the rabbit ACLT model is widely used, *in vivo* models are limited by the complex biological and mechanical contributions to PTOA and lengthy post-ACLT development times. The direct role of abnormal mechanics post-ACLT has yet to be elucidated.



## 1.5 Mechanics and Mechanobiology of Orthopaedic Devices

Implanted orthopaedic devices often carry significant mechanical loads and thus have implications for adjacent tissues and implant stability. The introduction of metallic implants in orthopaedics has made a tremendous impact on clinical practice, ranging from screws and pins to prosthetic replacement joints. However, a recognized complication notably in metallic hip implants was bone resorption around the implant, which could lead to implant loosening, requiring revision surgery [36]. This was theorized to be caused by stress shielding, in which rigid implants carry loads, leaving surrounding bone carrying minimal loads, resulting in bone resorption due to mechanically-modulated responses by cells [36].

Bone formation and remodeling involves mechanobiology, a complex process by which mechanical loads influence the osteogenic biological response. It has been proposed that with controlled loading *in vitro* or *in vivo*, strain amplitudes up to  $\sim 200\mu\epsilon$  (microstrain,  $10^{-6}$  strain) result in net bone resorption,  $\sim 200$ - $1500\mu\epsilon$  preserve bone homeostasis, and  $>1500\mu\epsilon$  promote bone formation [37, 38]. This principle, termed the Mechanostat, may have profound implications for long-term ingrowth of bone and thus implant stability for high load-bearing orthopedic implants. It had been proposed that osteocytes, which are mechanosensory cells in bone, are responsible for modulation of bone formation and resorption in response to the mechanical environment [39, 40]. However, the precise mechanism by which this occurs is not yet fully understood. With this mechanobiological basis, a number of modern designs for prosthetic hips and knees, as well as spine fusion implants have sought increased implant strains to promote adjacent tissue ingrowth.

## 1.6 Degenerative Disc Disease and Spinal Fusion Implants

Degenerative disc disease (DDD) is degeneration of the intervertebral disc, most commonly in the lumbar or cervical regions of the spine [41]. Lumbar disc degeneration is a common cause of low back pain with increasing age and can lead to neurological deficits secondary to nerve compression from bulging or extruded disc contents [42]. Whereas most cases of low back pain can be managed medically with supportive care and pharmacologic therapy, failure of conservative treatment may require surgical intervention to relieve pain. The mainstay of surgical treatment for lumbar DDD is interbody fusion, in which affected intervertebral disc(s) are removed and apposing vertebral bodies are fixed together with hardware with subsequent bony ingrowth to the implanted hardware [43]. Alternatively, total disc replacement, in which the native disc is surgically replaced by an artificial disc, has recently been used to treat lumbar DDD, but is relatively uncommon [43].

Lumbar spine interbody fusion implants, or cages, are used clinically to induce vertebral fusion as a treatment for DDD [44]. These cages provide mechanical support between vertebrae and are typically composed of polyether ether ketone (PEEK) or metal, such as titanium. Many cages are designed for usage with biologics, such as native or synthetic bone grafts, or growth factors including bone morphogenetic protein (BMP) [45-47]. More recently, spine cages have been designed to increase mechanical compliance and allow bony ingrowth by utilizing open-space lattice or truss structures [48]. Such complex designs can be manufactured with the advent of metallic 3-D printing, particularly titanium alloy.

## 1.7 References

1. Buckwalter JA, Mankin HJ. Articular cartilage. Part I: tissue design and chondrocyte-matrix interactions. *J Bone Joint Surg Am.* 1997;79-A:600-11.
2. Buckwalter JA, Mankin HJ, Grodzinsky AJ. Articular cartilage and osteoarthritis. *Instr Course Lect.* 2005;54:465-80.
3. Sophia Fox AJ, Bedi A, Rodeo SA. The basic science of articular cartilage: structure, composition, and function. *Sports Health.* 2009;1(6):461-8.
4. Johnson VL, Hunter DJ. The epidemiology of osteoarthritis. *Best Pract Res Clin Rheumatol.* 2014;28:5-15.
5. Buckwalter JA, Mankin HJ. Articular cartilage: degeneration and osteoarthritis, repair, regeneration, and transplantation. *Instr Course Lect.* 1998;47:487-504.
6. Glyn-Jones S, Palmer AJ, Agricola R, Price AJ, Vincent TL, Weinans H, Carr AJ. Osteoarthritis. *Lancet (London, England).* 2015;386(9991):376-87.
7. Sandell LJ, Aigner T. Articular cartilage and changes in arthritis. An introduction: cell biology of osteoarthritis. *Arthritis Res.* 2001;3(2):107-13.
8. Carbone A, Rodeo S. Review of current understanding of post-traumatic osteoarthritis resulting from sports injuries. *J Orthop Res.* 2017;35(3):397-405.
9. Brown TD, Johnston RC, Saltzman CL, Marsh JL, Buckwalter JA. Posttraumatic osteoarthritis: a first estimate of incidence, prevalence, and burden of disease. *J Orthop Trauma.* 2006;20(10):739-44.
10. Chalmers PN, Mall NA, Moric M, Sherman SL, Paletta GP, Cole BJ, Bach BR, Jr. Does ACL reconstruction alter natural history?: A systematic literature review of long-term outcomes. *The Journal of bone and joint surgery American volume.* 2014;96(4):292-300.
11. Buckwalter JA, Mankin HJ. Articular cartilage. Part II: degeneration and osteoarthrosis, repair, regeneration, and transplantation. *J Bone Joint Surg Am.* 1997;79-A:612-32.
12. Zantop T, Herbort M, Raschke MJ, Fu FH, Petersen W. The role of the anteromedial and posterolateral bundles of the anterior cruciate ligament in anterior tibial translation and internal rotation. *The American journal of sports medicine.* 2007;35(2):223-7.
13. Dejour H, Bonnin M. Tibial translation after anterior cruciate ligament rupture. Two radiological tests compared. *The Journal of bone and joint surgery British volume.* 1994;76(5):745-9.

14. Makhmalbaf H, Moradi A, Ganji S, Omid-Kashani F. Accuracy of lachman and anterior drawer tests for anterior cruciate ligament injuries. *The archives of bone and joint surgery*. 2013;1(2):94-7.
15. Lotz MK, Kraus VB. New developments in osteoarthritis. Posttraumatic osteoarthritis: pathogenesis and pharmacological treatment options. *Arthritis Res Ther*. 2010;12(3):211.
16. Anderson DD, Chubinskaya S, Guilak F, Martin JA, Oegema TR, Olson SA, Buckwalter JA. Post-traumatic osteoarthritis: Improved understanding and opportunities for early intervention. *J Orthop Res*. 2011;29(6):802-9.
17. Buckwalter JA, Brown TD. Joint injury, repair, and remodeling: roles in post-traumatic osteoarthritis. *Clin Orthop Relat Res*. 2004;(423):7-16.
18. Friel NA, Chu CR. The role of ACL injury in the development of posttraumatic knee osteoarthritis. *Clinics in sports medicine*. 2013;32(1):1-12.
19. Papannagari R, Gill TJ, Defrate LE, Moses JM, Petruska AJ, Li G. In vivo kinematics of the knee after anterior cruciate ligament reconstruction: a clinical and functional evaluation. *The American journal of sports medicine*. 2006;34(12):2006-12.
20. Potter HG, Jain SK, Ma Y, Black BR, Fung S, Lyman S. Cartilage injury after acute, isolated anterior cruciate ligament tear: Immediate and longitudinal effect with clinical/MRI follow-up. *Am J Sports Med*. 2012;40:276-85.
21. Lieberthal J, Sambamurthy N, Scanzello CR. Inflammation in joint injury and post-traumatic osteoarthritis. *Osteoarthritis and cartilage*. 2015;23(11):1825-34.
22. Sward P, Frobell R, Englund M, Roos H, Struglics A. Cartilage and bone markers and inflammatory cytokines are increased in synovial fluid in the acute phase of knee injury (hemarthrosis)--a cross-sectional analysis. *Osteoarthritis and cartilage*. 2012;20(11):1302-8.
23. Marks PH, Donaldson ML. Inflammatory cytokine profiles associated with chondral damage in the anterior cruciate ligament-deficient knee. *Arthroscopy*. 2005;21(11):1342-7.
24. Wang LJ, Zeng N, Yan ZP, Li JT, Ni GX. Post-traumatic osteoarthritis following ACL injury. *Arthritis research & therapy*. 2020;22(1):57.
25. Elsaid KA, Fleming BC, Oksendahl HL, Machan JT, Fadale PD, Hulstyn MJ, Shalvoy R, Jay GD. Decreased lubricin concentrations and markers of joint inflammation in the synovial fluid of patients with anterior cruciate ligament injury. *Arthritis Rheum*. 2008;58(6):1707-15.
26. Christiansen BA, Guilak F, Lockwood KA, Olson SA, Pitsillides AA, Sandell LJ, Silva MJ, van der Meulen MC, Haudenschild DR. Non-invasive mouse models of post-traumatic osteoarthritis. *Osteoarthritis and cartilage*. 2015;23(10):1627-38.

27. Yoshioka M, Coutts RD, Amiel D, Hacker SA. Characterization of a model of osteoarthritis in the rabbit knee. *Osteoarthritis Cartilage*. 1996;4:87-98.
28. Tochigi Y, Vaseenon T, Heiner AD, Fredericks DC, Martin JA, Rudert MJ, Hillis SL, Brown TD, McKinley TO. Instability dependency of osteoarthritis development in a rabbit model of graded anterior cruciate ligament transection. *J Bone Joint Surg Am*. 2011;93(7):640-7.
29. Sah RL, Yang AS, Chen AC, Hant JJ, Halili RB, Yoshioka M, Amiel D, Coutts RD. Physical properties of rabbit articular cartilage after transection of the anterior cruciate ligament. *J Orthop Res*. 1997;15:197-203.
30. Batiste DL, Kirkley A, Lavery S, Thain LM, Spouge AR, Gati JS, Foster PJ, Holdsworth DW. High-resolution MRI and micro-CT in an ex vivo rabbit anterior cruciate ligament transection model of osteoarthritis. *Osteoarthritis Cartilage*. 2004;12(8):614-26.
31. Batiste DL, Kirkley A, Lavery S, Thain LM, Spouge AR, Holdsworth DW. Ex vivo characterization of articular cartilage and bone lesions in a rabbit ACL transection model of osteoarthritis using MRI and micro-CT. *Osteoarthritis Cartilage*. 2004;12(12):986-96.
32. Kajabi AW, Casula V, Ojanen S, Finnila MA, Herzog W, Saarakkala S, Korhonen RK, Nissi MJ, Nieminen MT. Multiparametric MR imaging reveals early cartilage degeneration at 2 and 8 weeks after ACL transection in a rabbit model. *J Orthop Res*. 2020.
33. Ojanen SP, Finnila MAJ, Makela JTA, Saarela K, Happonen E, Herzog W, Saarakkala S, Korhonen RK. Anterior cruciate ligament transection of rabbits alters composition, structure and biomechanics of articular cartilage and chondrocyte deformation 2weeks post-surgery in a site-specific manner. *J Biomech*. 2020;98:109450.
34. Makela JT, Rezaeian ZS, Mikkonen S, Madden R, Han SK, Jurvelin JS, Herzog W, Korhonen RK. Site-dependent changes in structure and function of lapine articular cartilage 4 weeks after anterior cruciate ligament transection. *Osteoarthritis Cartilage*. 2014;22(6):869-78.
35. Roemhildt ML, Coughlin KM, Peura GD, Badger GJ, Churchill D, Fleming BC, Beynon BD. Effects of increased chronic loading on articular cartilage material properties in the lapine tibio-femoral joint. *J Biomech*. 2010;43(12):2301-8.
36. Huiskes R, Weinans H, van Rietbergen B. The relationship between stress shielding and bone resorption around total hip stems and the effects of flexible materials. *Clin Orthop Relat Res*. 1992;(274):124-34.
37. Frost HM. Bone's mechanostat: a 2003 update. *Anat Rec A*. 2003;275(2):1081-101.
38. Turner CH. Three rules for bone adaptation to a mechanical stimuli. *Bone*. 1998;23:399-407.

39. Bonewald LF. The amazing osteocyte. *J Bone Miner Res.* 2011;26(2):229-38.
40. Klein-Nulend J, Bacabac RG, Mullender MG. Mechanobiology of bone tissue. *Pathol Biol (Paris).* 2005;53:576-80.
41. Battie MC, Videman T. Lumbar disc degeneration: epidemiology and genetics. *The Journal of bone and joint surgery American volume.* 2006;88 Suppl 2:3-9.
42. Luoma K, Riihimaki H, Luukkonen R, Raininko R, Viikari-Juntura E, Lamminen A. Low back pain in relation to lumbar disc degeneration. *Spine.* 2000;25(4):487-92.
43. Yoshihara H, Yoneoka D. National trends in the surgical treatment for lumbar degenerative disc disease: United States, 2000 to 2009. *The spine journal : official journal of the North American Spine Society.* 2015;15(2):265-71.
44. Phillips FM, Slosar PJ, Youssef JA, Andersson G, Papatheofanis F. Lumbar spine fusion for chronic low back pain due to degenerative disc disease: a systematic review. *Spine.* 2013;38(7):E409-22.
45. Bishop RC, Moore KA, Hadley MN. Anterior cervical interbody fusion using autogeneic and allogeneic bone graft substrate: a prospective comparative analysis. *J Neurosurg.* 1996;85(2):206-10.
46. Burkus JK, Gornet MF, Dickman CA, Zdeblick TA. Anterior lumbar interbody fusion using rhBMP-2 with tapered interbody cages. *J Spinal Disord Tech.* 2002;15(5):337-49.
47. Agarwal R, Williams K, Umscheid CA, Welch WC. Osteoinductive bone graft substitutes for lumbar fusion: a systematic review. *J Neurosurg Spine.* 2009;11(6):729-40.
48. Kiapour A, Vijay G, Ferrara L, Hunt J, editors. Subsidence evaluation of 4-WEB, a novel cross strut based, interbody cage design. *International Society for the Study of the Lumbar Spine (ISSLS); 2011; Gothenburg, Sweden.*

## CHAPTER 2

# JOINT-SCALE MECHANO-PATHOLOGY IN POST- TRAUMATIC OSTEOARTHRITIS: EX VIVO IMPOSED GAIT- LIKE LOADING OF ACL-TRANSECTED RABBIT KNEES INDUCES ABNORMAL KINEMATICS AND CARTILAGE DEGENERATION

### 2.1 Abstract

#### *Background*

The clinical time course of degeneration due to mechanical and biological insults in post-traumatic osteoarthritis (PTOA) is complex and remains unclear. *In vivo* rabbit anterior cruciate ligament transection (ACLT) models for PTOA have demonstrated accelerated gross and histologic degeneration of knee cartilage.

#### *Hypothesis/Purpose*

Abnormal knee mechanics with ACLT in an *ex vivo* rabbit loading model leads to accelerated cartilage degeneration consistent with ACLT rabbits *in vivo*.

## ***Study Design***

Controlled Laboratory Study

## ***Methods***

*Ex vivo* loading experiments were performed to assess the effect of ACLT on rabbit knee (1) kinematics under both laxity and knee articulation loading schemes, (2) cartilage degeneration after knee articulation loading as assessed by gross reflectance and 3-D histology. New Zealand White rabbit knees were tested for anterior-posterior laxity under Normal (CTRL), Sham (SHAM), and ACLT conditions (N=4 each), as well as during cyclic flexion-extension loading to 500 and 1,000 cycles for SHAM and ACLT (N=3-4 each). India ink reflectance and 3-D histological imaging of femoral cartilage were compared with *in vivo* 4 weeks post-ACLT and intact control rabbit knees (N=10 each), with additional *ex vivo* unloaded control knees (N=10).

## ***Results***

Anterior drawer laxity increased with ACLT ( $4.07 \pm 0.43$ mm) compared with NL ( $0.76 \pm 0.14$ mm) and SHAM ( $0.86 \pm 0.21$ mm) at  $90^\circ$  flexion ( $p < 0.05$ ). Laxity was lower at  $135^\circ$ , compared to  $90^\circ$ , for all groups ( $p < 0.05$ ). During knee articulation, tibial anterior-posterior translation was higher in ACLT ( $0.68 \pm 0.26$ mm) compared to SHAM ( $0.33 \pm 0.15$ mm,  $p < 0.05$ ).

Lower India ink reflectance scores, indicative of higher surface damage, was seen in posterior regions of the MFC and LFC in ACLT knees at 1000 cycles, compared with SHAM and CTRL ( $p < 0.05$ ). Histopathological features of cartilage surface in vertical slices were asperities of less than 20  $\mu$ m in width (roughening and fibrillation) in loaded SHAM knees. At 500 cycles of loading, horizontal and vertical fissures of larger than 20  $\mu$ m length were seen in



addition to roughening and fibrillation. At 1000 cycles, more prominent vertical fissures and early erosions of the cartilage surface were observed.

### ***Conclusion***

Mechanically-induced cartilage degeneration with ACLT destabilization in this *ex vivo* rabbit study resembles *in vivo* surface damage, as reflected by india ink and histology. This suggests that abnormal loading in the absence of *in vivo* biological joint changes may serve as a driving force for early degeneration in PTOA.

### ***Clinical Relevance***

Increased cartilage degeneration after ACLT in the rabbit supports abnormal mechanical loading as a mechanism for accelerated development of PTOA after ACL injury.

## 2.2 Introduction

Osteoarthritis (OA) is driven by complex mechanical and biological processes at multiple time and length scales, often starting with cartilage surface damage. The mechanism underlying the accelerated degeneration of cartilage in post-traumatic osteoarthritis (PTOA) is unclear, and involves changes in both mechanical and biological factors [1]. Most commonly, tearing of the anterior cruciate ligament (ACL) leads to destabilization of the knee, particularly with increased anterior translation of the tibia and rotational instability [2]. The clinical time course of degeneration due to mechanical and biological insults is unclear, making the testing of mechanistic pathways difficult to study in humans.

In the ACL transection (ACLT) rabbit model, cartilage damage localizes to specific sites, but the direct role of abnormal mechanics is unclear [3]. *In vivo* rabbit studies have demonstrated accelerated gross and histologic degeneration of the knee cartilage at 4 and 8 weeks post-ACLT [4, 5]. Alterations of knee stability and mechanical properties of cartilage have been demonstrated in the rabbit [5, 6]. *Ex vivo* micro-CT and MRI studies have described 3-D structural changes in cartilage and underlying osseous tissues at 2, 4, and 8 weeks post-ACLT [7-9]. Recently, ACLT has demonstrated alterations in composition, structure, and biomechanics of articular cartilage at both 2 weeks and 4 weeks after rabbit ACLT [10, 11]. Mechanical overloading has been suggested as a driving factor for alterations in cartilage material properties in an *in vivo* overload model [12]. Although the rabbit ACLT model is widely used, *in vivo* models are limited by the complex biological and mechanical contributions to PTOA and lengthy post-ACLT development times. Isolation of the mechanical component of cartilage degeneration would be a useful approach to elucidating pathways to development of PTOA.

Mechanical testing systems have been developed for *ex vivo* loading of human and rabbit knees. The Oxford Rig allowed *ex vivo* loading of human knees replicate kinematics of physiologic activities such as cycling or climbing stairs with simultaneous mechanical characterization [13]. Later developed systems added the capacity to mimic quadriceps and hamstrings muscle loads via suture lines and electromechanical actuators [14-16]. Further refined systems added optical tracking of the femur, tibia, and patella for improved positional tracking and enabling modeling with pre-testing 3-D imaging [17-19]. Using a similar electromechanical approach, rabbit knee laxity has been characterized before and after ACLT in rabbits, both *in vivo* and *ex vivo*. Disruption of the ACL resulted in increased anterior displacement, with preserved posterior displacement [5, 20-22]. In these studies, knee flexion angles of 90° and 135° were used during laxity testing to represent habitual weight-bearing positions in the rabbit. Whereas these studies establish a mechanical basis for PTOA, they are limited to mechanical assessment, rather than mechanical induction of degenerative wear.

Dynamic loading through the hop cycle of rabbits demonstrates differences from the human gait cycle. The rabbit gait exhibits higher flexion angles throughout the hop cycle [23]. Loading profiles through the rabbit hop cycle are not largely studied, and have used a combination of experimental force and motion data with mechanical modeling to estimate muscle loads [24, 25]. During hopping, the peak loads generated by the primary force-developing muscles of the knee were predicted to be 300% body weight (BW) for the quadriceps and 150% BW for the gastrocnemius [24]. This equates to 103N and 52N load, respectively, for a typical 3.5kg skeletally mature NZW rabbit in the quadriceps and gastrocnemius, respectively. These studies suggest that the primary antagonistic muscles groups during the hop cycle are the quadriceps and gastrocnemius, with a minor role of the hamstrings.

We hypothesized that abnormal knee mechanics with ACLT in an *ex vivo* rabbit loading model leads to accelerated cartilage degeneration consistent with ACLT rabbits *in vivo*. In this study, we aimed to assess kinematics and both gross and histological degeneration after cyclic gait loading in ACLT rabbit knees, compared with *ex vivo* loaded SHAM and *in vivo* ACLT and CTRL knees.

## 2.3 Methods

### *Study Design*

*Ex vivo* loading experiments were performed to assess the effects of ACLT on post-mortem and previously -80°C frozen adult New Zealand White rabbit knees (N=24). Experiments evaluated (1) knee laxity at fixed joint angles and kinematics during knee articulation, and (2) cartilage surface damage by india ink staining and 3-D histology (**Fig. 2.1**). An additional cohort of *in vivo* 4 weeks post-ACLT rabbits (N=10) was analyzed for surface damage.

### *Effect of ACLT on rabbit knee laxity and kinematics*

#### *Knee Laxity*

Anterior and posterior drawer laxity were compared for knees (N=4) that were (A) Normal (NL), (B) Sham-operated (SHAM), and (C) ACLT. Laxity testing ( $\pm 75$ N) was performed before and sequentially after SHAM and ACLT surgeries, at physiological rabbit knee flexion angles of 90° and 135°. SHAM controlled for surgery by exposing and closing the joint (without ACLT). Absolute changes in laxity with each surgery were compared by 1-way ANOVAs with post-hoc Tukey tests.

Sample Preparation: Rabbit knees were dissected to retain synovial structures, subjected to either ACLT or SHAM surgery, and mounted on a mechanical testing system. Intact rabbit knees were dissected clean of skin, muscle, and fascial tissues, retaining the knee ligaments and synovial capsule intact. For the SHAM and ACLT groups, a single 5mm medial parapatellar

arthrotomy was made with 2-pass suture closure (4-0 polyglycolic acid) of the synovial capsule and overlying skin. For ACLT, the ACL was visualized and transected using curved scissors. ACLT was verified by manual anterior drawer. The distal femur and proximal tibia were each affixed with spherical fiducial beads (3/16" diameter) using cyanoacrylate to the cortical surface for video tracking. Femoral and tibial shafts were potted in cement and rigidly mounted on a mechanical testing system (Mach-1™ V500, Biosyntech Canada, Montreal) to displace the tibia in the anterior/posterior direction (**Fig. 2.2A,B**).

Mechanical Loading: Knees were repeatedly loaded with an ACL laxity testing routine as unloaded control, and after SHAM and ACLT surgeries. Loading consisted of two sets of four consecutive laxity cycles of  $\pm 75\text{N}$  anterior/posterior at  $0.5\text{mm/s}$  for knee flexion angles of  $90^\circ$  and  $135^\circ$ . Each cycle was a sequence of anterior pull of the tibia (displacement control,  $0.5\text{mm/s}$ ) to  $+75\text{N}$ , followed by posterior push of the tibia (displacement control,  $0.5\text{mm/s}$ ) to  $-75\text{N}$ , with a return to  $0\text{N}$ . This sequence was immediately repeated for a total of 4 cycles. An initial set of cycles was used for pre-conditioning and finding the "neutral position" of the joint for the second set of cycles. The last cycle of the second set was used for data analysis. After each complete test routine, surgeries were sequentially performed *in situ* while the rabbit was mounted in the testing system. Tissues were kept moist with phosphate-buffered saline (PBS) + protease inhibitor ( $50\text{mM EDTA-Na}_2$ ).

Laxity Analysis: Affixed fiducial markers were video tracked and analyzed to track tibial anterior-posterior displacement during the loading cycle. Fiducial markers were video recorded using a camera (D7100 with  $105\text{mm f/2.8}$  macro lens, Nikon, Tokyo, Japan) with an in-frame scale bar. Marker position was tracked by color (RGB) thresholding to select a region of interest (ROI) for each marker in video still-frame images. Each ROI was morphologically closed

(round, radius: 4px) and centroids (x,y) were determined in MATLAB (R2019a, MathWorks, Natick, USA). Femoral and tibial fiducial centroids, and corresponding distance between centroids, were computed at 0N, +75N, and -75N from video still images. Laxity was computed as the change in anterior-posterior inter-fiducial distance from 0 to +75N (anterior), 0 to -75N (posterior), and +75N to -75N (A-P). Changes in laxity with treatment (SHAM, ACLT) from NL were computed.

### *Ex Vivo Knee Articulation*

*Ex vivo* rabbit knees (N=10) underwent cyclic knee extension-flexion loading after (A) SHAM or (B) ACLT operation, loaded with 500 or 1,000 cycles (N=2-3 each). A-P translation was assessed by video imaging and analysis, and compared by 1-way ANOVA with post-hoc Tukey tests.

Sample Preparation: Rabbit knees were partially dissected clean of skin, thigh muscle groups, and fascial tissues, retaining the tissues distal to the knee (including leg muscles), knee ligaments, and synovial capsule intact. For the SHAM and ACLT groups, a single 5mm medial parapatellar arthrotomy was made with layered closure of synovial capsule (two interrupted sutures) and overlying skin (three interrupted sutures) using 4-0 polyglycolic acid suture. The capsule was further sealed by applying a coating of tissue adhesive (VetBond, 3M, St. Paul, USA) over the incision. For ACLT, the ACL was visualized and transected using curved scissors, then verified by manual anterior drawer. Osseous tunnels (1-1.5mm diameter) were drilled through the distal femur (anterior-posterior tunnel), patella (medial-lateral tunnel), and distal tibia (medial-lateral tunnel) to allow application of tensile loads via loading lines to mimic muscle contractions. The distal femur, proximal tibia, and distal tibia were each affixed with

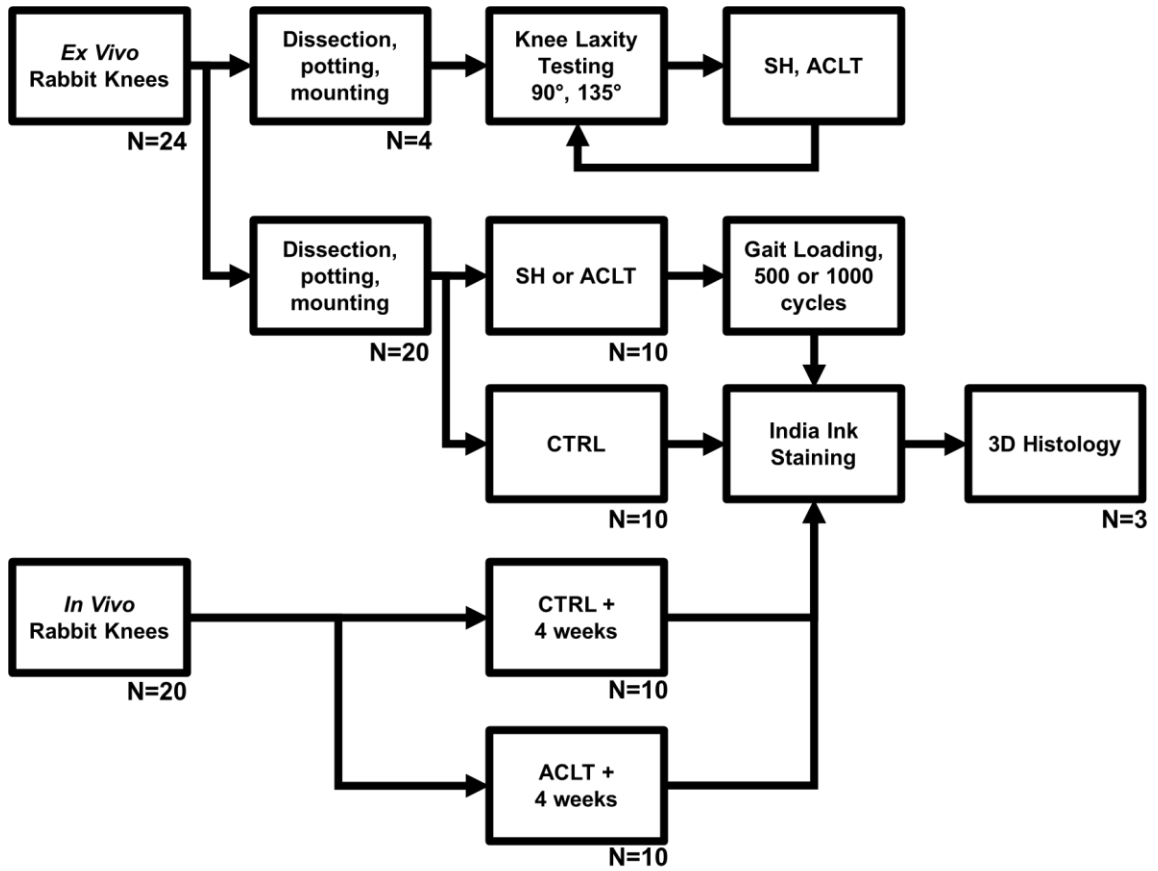
fiducial beads (1/4" diameter) using cyanoacrylate to the cortical surface for video tracking anterior-posterior translation. The femoral shaft was potted in cement and rigidly mounted to a custom loading apparatus for knee articulation (**Fig. 2.2C-F**). In this configuration, the femur was rigidly mounted, whereas the tibia was not constrained.

Mechanical Loading: Cyclic loading was applied via tensioning/relaxing loading lines through osseous tunnels to mimic loading induced by the quadriceps and gastrocnemius. High-load (30kg) braided fishing line (PowerPro Spectra, Shimano, Irvine, USA) was threaded through osseous tunnels to approximate the *in vivo* load direction of the quadriceps (patellar tunnel to proximal femur) and gastrocnemius (distal tibia to distal femur). Tensile loads were generated by high-torque (3 N-m) stepper motors retracting each tensile line, with load-controlled feedback from load cells (25kg capacity). Low-friction pulleys were used to redirect tensile lines. Load sequence was controlled by custom software in LabVIEW (v2018, National Instruments, Austin, USA) to be cyclic alternating ramp-relax loads to 100N for quadriceps (knee extension) then 50N for gastrocnemius (knee flexion) at a cycle rate of 0.75Hz. Tissues were continuously drip irrigated with phosphate-buffered saline (PBS) with 5mM EDTA protease inhibitor.

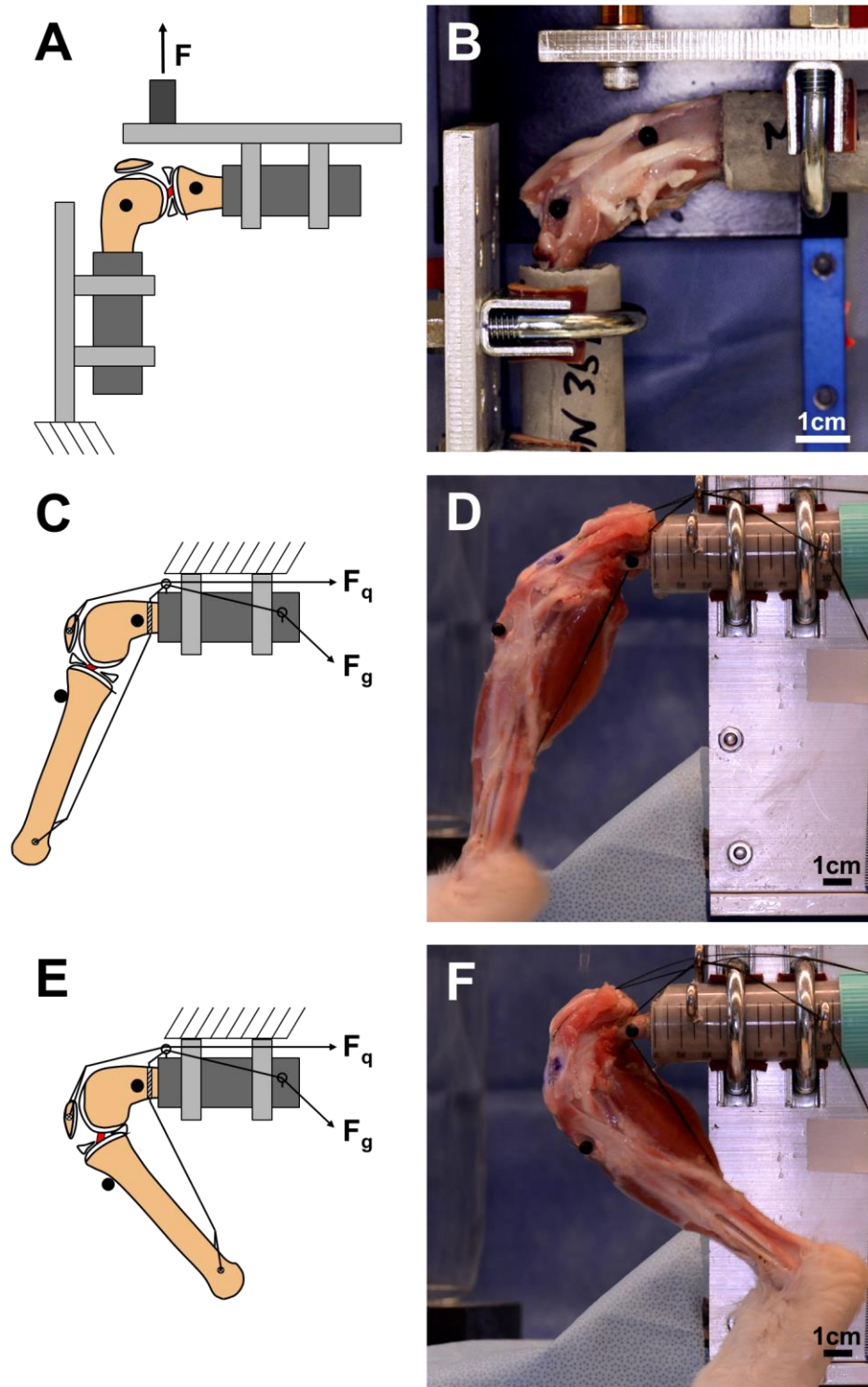
A-P Translation: Affixed fiducial markers were video tracked from a sagittal angle during loading and analyzed to track tibial anterior-posterior during the loading cycle. Fiducial markers were video recorded using a camera (D7100 with 105mm f/2.8 macro lens, Nikon, Tokyo, Japan) with in-frame scale bars. Marker position was tracked by color (RGB) thresholding to select a region of interest (ROI) for each marker in video still-frame images in MATLAB. Each ROI was morphologically closed (round, radius: 4px) and centroids (x,y) were determined. Femoral and tibial fiducial centroids, and corresponding anterior-posterior tibial displacement, were computed



at the initial (0 cycles) and final (500 or 1000 cycles) period. Tibial A-P displacement was determined as the change in A-P distance between extension phase and flexion phase at 135° knee flexion angle.



**Figure 2.1: Study design.** Sample interventions (CTRL, SHAM, ACLT) and assessments for rabbit knees.



**Figure 2.2: Mechanical loading setup.** Loading schematics and gross images for *ex vivo* (A,B) laxity testing, and knee articulation in (C,D) extension and (E,F) flexion. Arrows indicate directions of force ( $F$ ), quadriceps force ( $F_q$ ), and gastrocnemius force ( $F_g$ ).

### ***Effect of ACLT on rabbit knee cartilage surface damage***

After *ex vivo* cyclic extension-flexion loading, rabbit knees (N=10) were assessed for surface damage by india ink staining and histology. Surface damage via quantification by India ink reflectance score was determined for ACLT at 500 and 1,000 cycles (N=3 per group) and compared with CTRL (N=10), SHAM at 500 and 1,000 (N=4 total, grouped for analysis) cycles, and with a separate 4-week saline injected *in vivo* ACLT and CTRL cohort (N=10) by 2-way ANOVA with *post-hoc* Tukey tests. Surface features, including roughening, fibrillation, horizontal and vertical fissures, and erosions were assessed in two orthogonal vertical section orientations from 3-D histology.




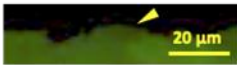

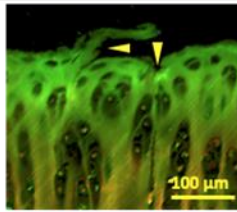



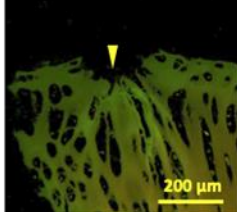
*In vivo* Cohort Surgery: With IACUC approval, mature adult female New Zealand White rabbits (N=10) were subjected to unilateral ACLT in the right knee via the parapatellar approach, with left knee as non-operated CTRL. ACLT knees received 0.3 mL injections of saline on days 2, 4, 7, 14 and 21 post-surgery. Femoral condyles were harvested on day 28 post-ACLT, and frozen at -20°C until further analysis.

High Resolution Digital Imaging of India Inked Surface (HiReD-IIIS) Analysis: Quantitative reflectance scores were determined for each femoral condyle articular cartilage as described elsewhere. Briefly, areas of 20 x 16 mm<sup>2</sup> cartilage surface were imaged under standardized positioning and lighting conditions using a digital camera and macro lens (D7100 with 105mm f/2.8 macro lens, Nikon, Tokyo, Japan). Images were normalized using standard gray scale targets (Q13, Eastman Kodak Co., Rochester, NY, U.S.A) with reflectance of light from normal, unstained cartilage considered as 1, and damaged, maximally ink-stained cartilage as 0. The reflectance of light from the surface was calculated as a direct correlate of surface

damage in the weight-bearing postero-medial (PostMed) and postero-lateral (PostLat), and non-weight-bearing antero-medial (AntMed) and antero-lateral (AntLat) femoral cartilage defined by an averaged, shrunk mask of each site.

Histological Analysis of Surface Features: Cartilage matrix features (roughening, fibrillation, horizontal and vertical fissures, and erosions) were qualitatively graded in anterior-posterior and medial-lateral planes. To visualize microscopic features of damage in depth, osteochondral blocks (OCBs) from the posteromedial location on SHAM (500 cycles) and ACLT (500 and 1000 cycles) femoral condyles were imaged by Digital Volumetric Imaging (DVI) as described previously [26]. Briefly, whole femoral condyles were fixed with 4% paraformaldehyde in PBS, and demineralized with 20% formic acid (Shandon TBD-2). 1.8 x 1.8 x 3 mm<sup>3</sup> OCBs were harvested from matching regions on SHAM and ACLT FCs. OCBs were stained for matrix (0.1% Eosin Y, pH = 5) and cell nuclei (0.1% Acridine Orange in 0.01M citrate buffer, pH = 5), embedded in Spur resin with Sudan Black opacifier, and imaged at (0.88 μm)<sup>3</sup> voxels with a Nikon (Tokyo, Japan) E600 fluorescence microscope with a 310 Plan Apochromat objective (NA 0.45). Three-dimensional renderings were visualized in RESView 3.0 software (Resolution Sciences Corporation) and 2-D cross-sections of image stack were exported as high-resolution bitmaps via MATLAB. Lesions from the transverse (TRA) plane of DVI images were registered to those of HiReD-IIIs images. The corresponding traditional vertical (Coronal = COR, Sagittal = SAG) views of the lesions in ACLT and matched CTRL samples were obtained as 500 x 500 μm<sup>2</sup> area representations. Cartilage features were identified according to semi-quantitative definitions addressing zone-specific early-stage feature dimensions and frequency (**Table 2.1**). The definitions were adapted from classical histopathological grading systems (OARSI, Mankin) and adjusted for rabbit cartilage thickness.

**Table 2.1: Cartilage grading system.** Histopathological feature definitions of articular cartilage structure.

#	FEATURE	DEPTH	Grade	DEFINITION	EXTENT RT WIDTH	SCALE		
1	Roughness	Sur	1	smooth	asperities with depth <2 μm, width 0-2 μm	≥ 50%	 5 μm	 5 μm
			2	rough	asperities with depth >2 μm, width 2-8 μm			
			3	no AC	no AC	100%		
2	Fibrillation	Sur	1	none	asperities with depth <2 μm, width <8 μm	≥ 50%	 20 μm	 20 μm
			2	fibrillated	asperities with depth >2 μm, width 8-20 μm			
			3	no AC	no AC	100%		
3	Horizontal Fissures	FT	1	none	crack(s) oriented 0-45°, with length <20 μm	100%	 100 μm	
			2	horizontal	crack(s) oriented 0-45°, with length >20 μm			
			3	no AC	no AC	100%		
4	Vertical Fissures	FT	1	none	crack(s) oriented 45-90°, with length 0-200 μm	100%	 100 μm	 100 μm
			2	vertical	crack(s) oriented 45-90°, with length >200 μm			
			3	no AC	no AC	100%		
5	Cartilage Erosion	FT	1	none	AC thickness 100% of reference	100%	 200 μm	 200 μm
			2	mild	AC thickness 90-100% of reference			
			3	moderate	thickness of AC of 50-90% of reference	≥ 50%		
			4	severe	thickness of AC of 0-50% of reference			
			5	complete	no AC			

## 2.4 Results

### *Effect of ACLT on rabbit knee laxity and kinematics*

#### *Knee Laxity*

Anterior and A-P drawer distances increased with ACLT compared with NL and SHAM ( $p < 0.05$ , **Fig. 2.3A-C**). Drawer distances were decreased at  $135^\circ$ , compared to  $90^\circ$ , for all groups ( $p < 0.05$ ). Anterior drawer distances at  $90^\circ$  were  $0.76 \pm 0.14$ mm (mean $\pm$ SD),  $0.86 \pm 0.21$ mm, and  $4.07 \pm 0.43$ mm for NL, SHAM, and ACLT, respectively, and  $0.37 \pm 0.09$ mm,  $0.39 \pm 0.09$ mm, and  $2.21 \pm 0.39$ mm at  $135^\circ$  for NL, SHAM, and ACLT, respectively. Anterior-posterior (A-P) drawer distances at  $90^\circ$  were  $1.92 \pm 0.27$ mm,  $1.96 \pm 0.39$ mm, and  $5.43 \pm 0.29$ mm for NL, SHAM, and ACLT, respectively, and  $1.03 \pm 0.23$ mm,  $1.05 \pm 0.25$ mm, and  $3.08 \pm 0.43$ mm at  $135^\circ$  for NL, SHAM, and ACLT, respectively.

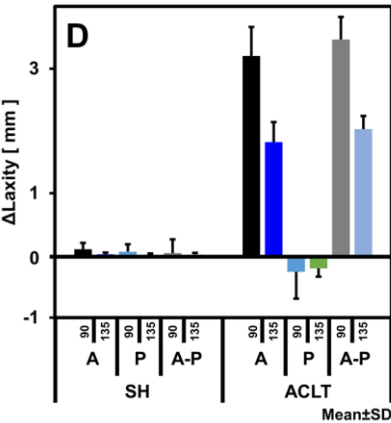
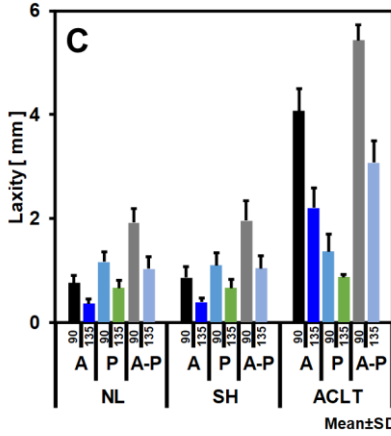
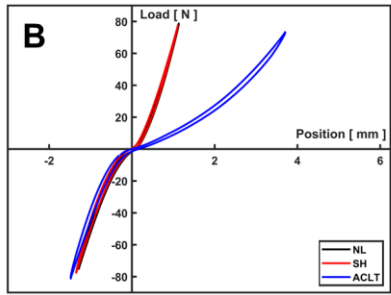
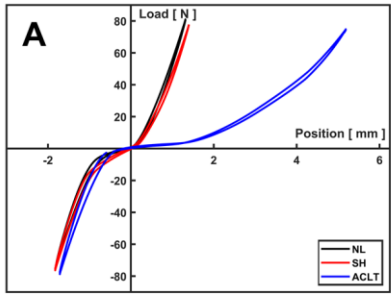
Posterior drawer distances were similar between all groups at  $90^\circ$  ( $p = 0.37$ ). and  $135^\circ$  ( $p = 0.08$ ). Posterior drawer distances at  $90^\circ$  were  $1.16 \pm 0.19$ mm,  $1.10 \pm 0.23$ mm, and  $1.36 \pm 0.34$ mm for NL, SHAM, and ACLT, respectively, and  $0.67 \pm 0.15$ mm,  $0.66 \pm 0.16$ mm, and  $0.87 \pm 0.06$ mm at  $135^\circ$  for NL, SHAM, and ACLT, respectively.

Changes in anterior and anterior-posterior (A-P) drawer distances increased from SHAM to ACLT ( $p < 0.05$ , **Fig. 2.3D**). Anterior drawer distance was increased at  $90^\circ$  for ACLT ( $3.21 \pm 0.46$ mm) compared to SHAM ( $0.10 \pm 0.10$ mm), and at  $135^\circ$  for ACLT ( $1.82 \pm 0.32$ mm) compared to SHAM ( $0.02 \pm 0.03$ mm). Anterior-posterior (A-P) drawer distance was increased at  $90^\circ$  for ACLT ( $3.47 \pm 0.36$ mm) compared to SHAM ( $0.04 \pm 0.22$ mm), and at  $135^\circ$  for ACLT ( $2.03 \pm 0.21$ mm) compared to SHAM ( $0.02 \pm 0.03$ mm).

### *Ex vivo Knee Articulation*

*Ex vivo* gait kinematics were affected by ACLT, with tibial A-P translation of SHAM ( $0.33\pm 0.15\text{mm}$ ) higher compared with ACLT ( $0.68\pm 0.26\text{mm}$ ,  $p<0.05$ ) at the initial state. ACLT A-P translation remained relatively unchanged at 500 cycles ( $0.84\pm 0.25\text{mm}$ ,  $p=0.92$ ) and 1000 cycles ( $0.65\pm 0.22\text{mm}$ ,  $p=0.99$ ). SHAM A-P translation was similarly unchanged at 500 cycles ( $0.22\pm 0.28\text{mm}$ ,  $p=0.99$ ) and 1000 cycles ( $0.21\pm 0.06\text{mm}$ ,  $p=0.99$ ).





**Figure 2.3: Laxity Testing.** Typical load-displacement curves for NL, SHAM (SH), and ACLT at (A) 90° and (B) 135° knee flexion. Laxity measures (C) and changes in laxity from NL (D) for Anterior (A), Posterior (P), and Anterior-Posterior (A-P) laxity at 90° and 135° knee flexion.

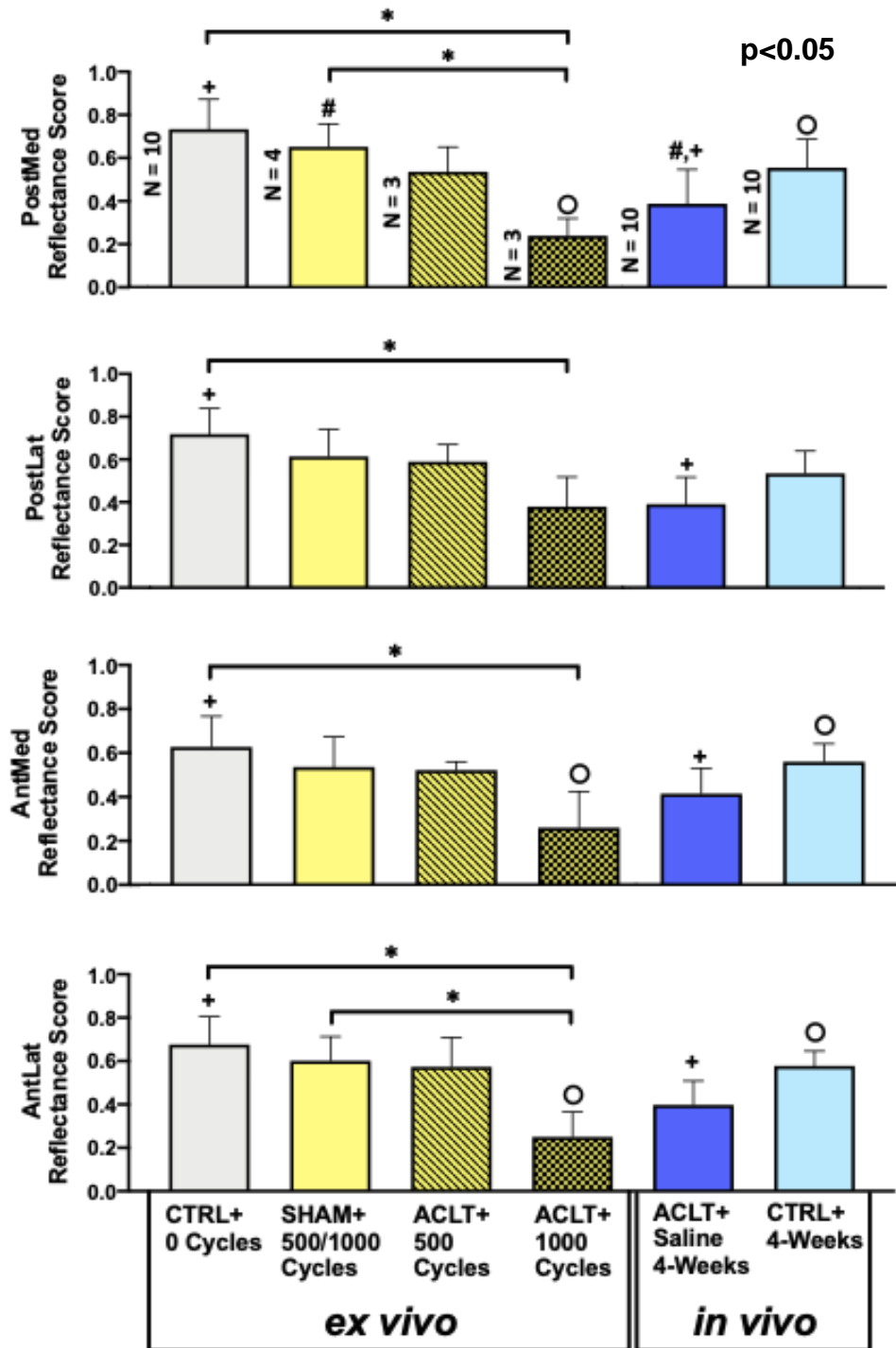
### ***Effect of ACLT on rabbit knee cartilage surface damage***

Cartilage showed increased surface damage on india ink reflectance with *ex vivo* cycling of ACLT knees, similar to *in vivo* ACLT knees (**Fig. 2.4**). The reflectance score (RS), inversely related to AC surface damage, was lower ( $p < 0.01$ ) at all regions for 1000 cycle ACLT group (PostMed  $0.24 \pm 0.14$ , PosLat  $0.38 \pm 0.24$ , AntMed  $0.26 \pm 0.28$  and AntLat  $0.25 \pm 0.20$ ) compared to non-loaded CTRL (PostMed  $0.73 \pm 0.14$ , PosLat  $0.72 \pm 0.12$ , AntMed  $0.63 \pm 0.14$  and AntLat  $0.68 \pm 0.12$ ) and SHAM (PostMed  $0.65 \pm 0.21$ , PostLat  $0.61 \pm 0.25$ , AntMed  $0.54 \pm 0.27$ , AntLat  $0.60 \pm 0.22$ ). Although not statistically significant, RS had a decreasing trend on all locations in 500 cycle ACLT (PostMed  $0.54 \pm 0.20$ , PostLat  $0.59 \pm 0.14$ , AntMed  $0.52 \pm 0.06$ , AntLat  $0.58 \pm 0.23$ ) compared to non-loaded CTRL, and SHAM. Loaded SHAM knees had similar reflectance score to those of non-loaded CTRLs, as well as *in vivo* 4-week post-ACLT contralateral CTRLs ( $p = 0.18-0.99$ ). *Ex vivo* loading at 1000 cycles caused damage that was comparable to those seen *in vivo* at 4-week post-ACLT at all locations ( $p = 0.60-0.99$ ).

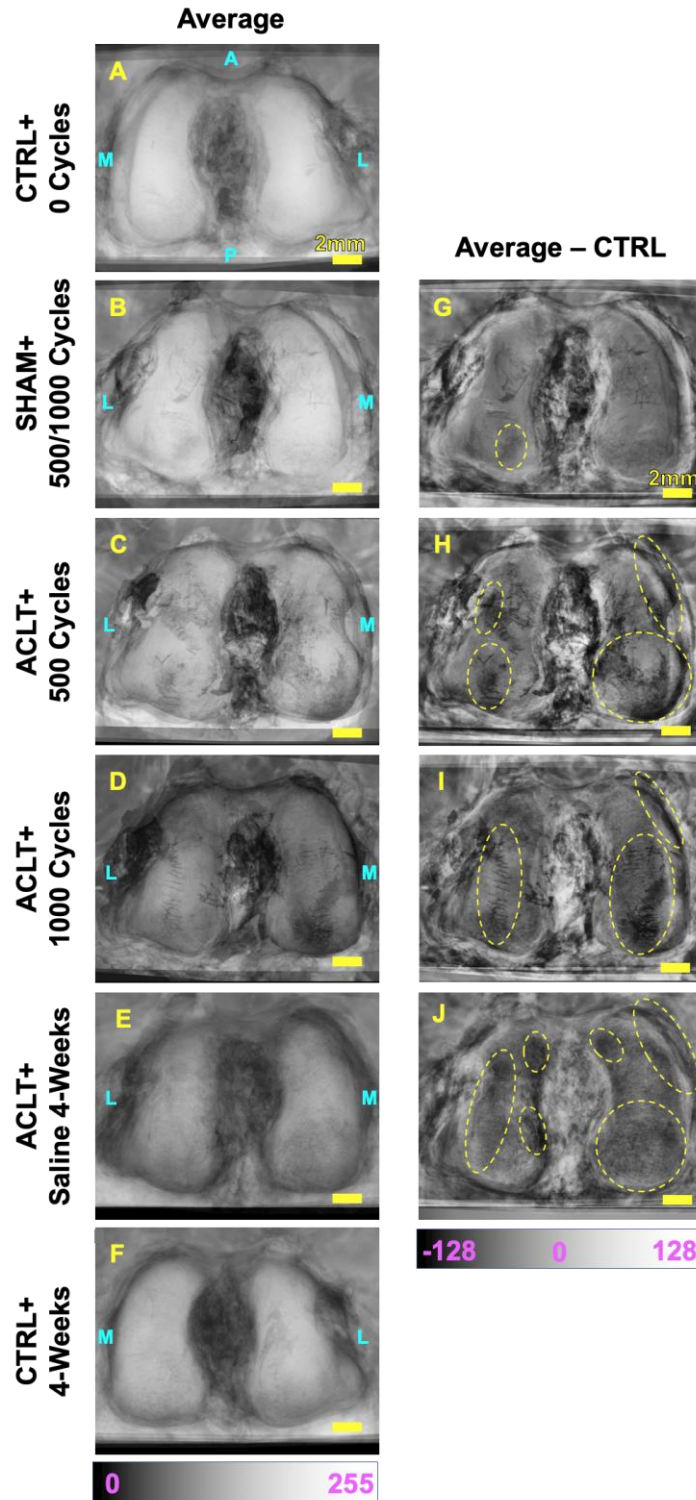
Digitally-averaged (**Fig. 2.5A-F**), and -subtracted (**Fig. 2.5G-J**) HiReD-IIIS images of ACLT FCs from CTRL in *ex vivo* and *in vivo* revealed specific regions that show ACLT- and mechanically-induced degeneration. Minimal surface India Ink staining was observed in PostLat of SHAM group (**Fig. 2.5G**). ACLT+500 and ACLT+1000 cycles groups showed similar regions of surface degeneration (PostMed, PostLat, and AntLat) with higher Ink staining at 1000 cycles (**Fig. 2.5H-I**). Qualitative comparison of ACLT and CTRL FCs *in vivo* indicated marked degeneration in the PostMed, PostLat, and AntLat regions, and to a lesser extent, the AntMed aspect (**Fig. 2.5J**).

Surface damage on HiReD-IIIS images mapped to histopathological matrix features. In SHAM FCs, the diffuse dark ink staining (**Fig. 2.6A,D,G,J**) mapped to roughening (asperities of

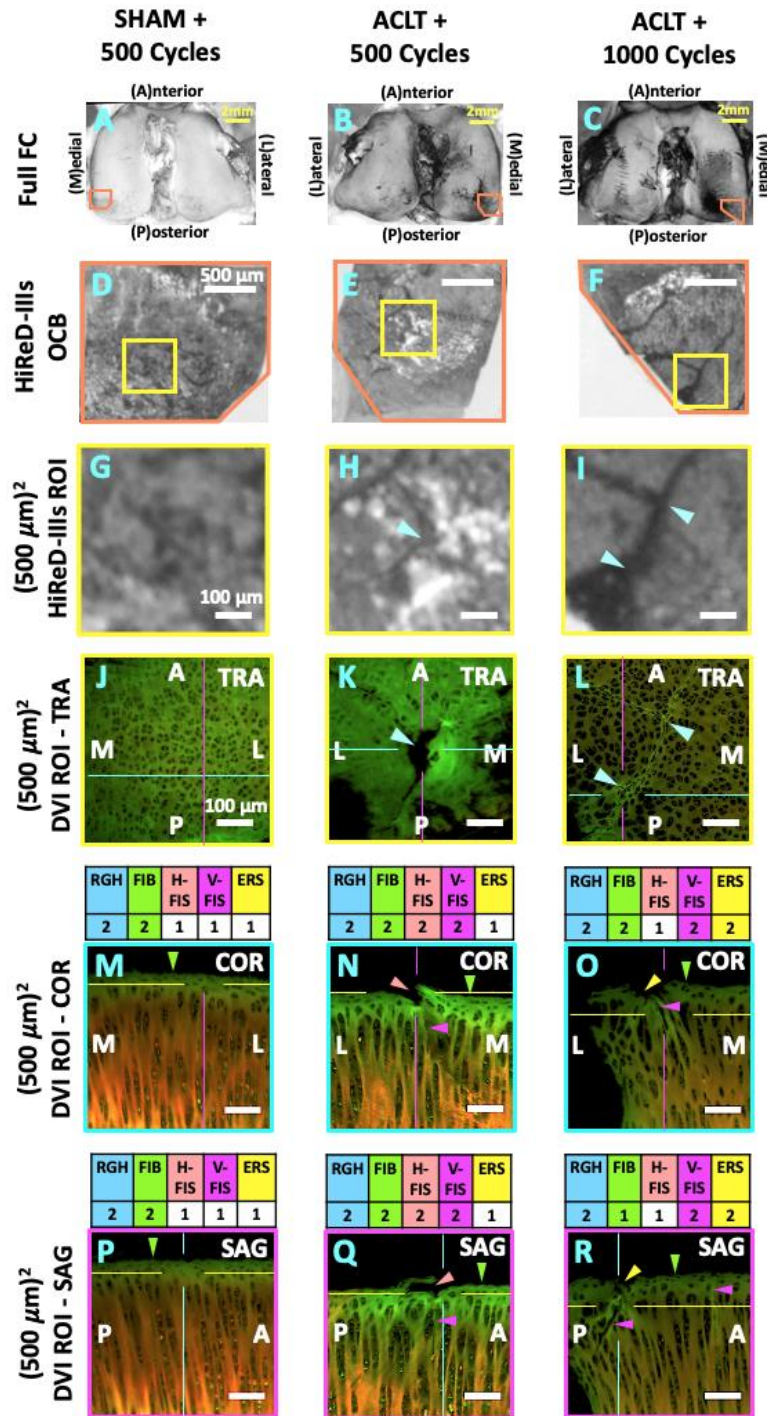
<8  $\mu\text{m}$  width) and fibrillation (asperities of 8-20  $\mu\text{m}$  width) of the articular surface in the anterior-posterior (A-P) and medial-lateral (M-L) directions on histological sections (**Fig. 2.6P,S**). At 500 and 1000 cycles, distinct interconnected damage patterns were detected on India inked ACLT FCs (**Fig. 2.6B,E,H,K and C,F,I,L**). At 500 cycles, horizontal fissures (cracks oriented 0-45 degrees, >20  $\mu\text{m}$  length) were evident in conjunction with what appeared as initiation of vertical fissures (**Fig. 2.6Q,T**). At 1000 cycles, well defined vertical fissures (cracks oriented 45-90 degrees, >20  $\mu\text{m}$  length) that extended into the deep zone were more prominent, in addition to erosion of the surface layer in both A-P and M-L directions (**Fig. 2.6R,U**). Roughening and fibrillation in the surface layer were seen in ACLT knees independent of cycle number.



**Figure 2.4: Regional India ink reflectance scores.** India Ink reflectance scores at postero-medial (PostMed), postero-lateral (PostLat), antero-medial (AntMed), and antero-lateral (AntLat) regions of femoral cartilage for not-loaded CTRL (N=10), SHAM (N=1 at 500, N=3 at 1000 and N=2 at 3000 cycles), and ACLT (500 and 1,000 cycles). Typical *in vivo* (N=10) reflectance scores at 4 weeks post-ACLT and CTRL shown for reference. Markers indicate significance ( $p < 0.05$ ).



**Figure 2.5: Areas of cartilage surface degeneration by HiReD-IIIS.** (A-F) Digitally-averaged and (G-J) digitally subtracted images of *ex vivo* and *in vivo* FCs from their respective CTRLs. A = Anterior, P = Posterior, M = Medial, and L = Lateral.



**Figure 2.6: Multi-scale imaging of cartilage degeneration.** Representative appearances of postero-medial femoral cartilage degeneration after india ink staining for (A,D,G) SHAM+500 cycles, (B,E,H) ACLT+500 cycles, and (C,F,I) ACLT+1,000 loading cycles. Volumetric (3-D) histology showing corresponding degeneration features in the (J,K,L) transverse (TRA) (M,N,O) coronal (COR), and (P,Q,R) sagittal (SAG) planes. Anterior (A), Posterior (P), Medial (M), and Lateral (L) aspects are noted.

## 2.5 Discussion

In this study, an *ex vivo* mechanically-driven PTOA rabbit model demonstrated abnormal knee kinematics and cartilage surface damage in ACLT compared with SHAM and CTRL knees. *Ex vivo* ACLT rabbit knees demonstrated increased A-P laxity at fixed flexion angles and higher A-P translation during knee articulation. India ink reflectance scoring and 3-D histology of *ex vivo* ACLT rabbit knees exhibited cartilage degeneration with knee articulation, consistent with *in vivo* 4-week post-ACLT rabbit knees.

The *ex vivo* loading approach has a number of differences compared with *in vivo* gait. Loading was simplified to represent the two primary antagonistic muscles in the rabbit hop, omitting the minor contributing muscle groups used in gait. The relative contribution by other muscle groups *in vivo* may be altered after ACLT, which was not investigated. The loading pattern was also simplified as sequential ramp/relax cycles for the quadriceps and gastrocnemius, as the time course of load magnitudes through the hop cycle is not well understood for the rabbit. Joint lubrication was provided only by the endogenous synovial fluid present at time of sacrifice, with no additional lubricant supplementation during loading. As this study's approach focused on mechanically-driven wear, the complex biological response leading to PTOA *in vivo* was not considered.

Rabbit knee laxity measures found in this study are consistent with and extend findings of previous studies, with increased anterior laxity and preserved posterior laxity after ACLT. The findings of higher laxity at 90° knee flexion compared with 135° for all groups is consistent with past studies. Similar laxity measures between normal and SHAM surgery groups demonstrate minimal mechanical compromise of the synovial tissues during SHAM surgery. This study uses the novel approach of measuring knee laxity by video tracking fiducial markers mounted to the

distal femur and proximal tibia. This tracking method accounts for compliance of the test system fixturing and specimen, which can substantially impact platen-to-platen displacement measures.

Altered kinematics during cyclic loading of ACLT knees were consistent with knee destabilization analogous to ACL tear. An increase in anterior-posterior translation in both benchtop laxity tests and knee articulation loading aligns with the primary mechanical function of the ACL, and supports a mechanism of increasing sliding and shear loads leading to increased cartilage degeneration. A lack of progression in A-P laxity with load cycle number in either SHAM or ACLT suggests that minimal further ligamentous damage occurs over the course of this loading approach.

Abnormal knee loading may serve to initiate cartilage damage and subsequent propagation of cartilage fibrillation and fissures. The increased sliding motion and shear loads in the cartilage could cause a localized mechanical failure in the superficial collagen network. This defect would serve a nidus for further crack propagation with continued loading, ultimately leading to additional stress concentrations and thus further failure points.

Mechanical induction of cartilage degeneration approximated the macroscopic and histological wear regions and progression recognized with *in vivo* ACLT studies. Higher surface degradation both with ACLT and higher cycle count, particularly on the MFC, mirrors the trends of surface roughening demonstrated *in vivo* at 4-week and 8-week post-ACLT. The increased strain due to the tibial anterior shift could induce increased stress in the tissue, disorganization and breakage of collagen network, manifesting as fibrillation and fissures. It is proposed that substantial mechanical loading alone can induce considerable cartilage degeneration, independent of potential biodegradative factors after ACLT. Further study is warranted in the



pattern and propagation of cartilage degeneration in the rabbit, analogous to erosion patterns recognized in the human knee.

These results suggest that *ex vivo* mechanical loading of ACLT knees can directly cause cartilage deterioration in the absence of biological alterations. Local abnormalities in contact and sliding may initiate damage patterns, similar to those in humans. Here, chondrocyte and matrix metabolism mechanisms that may accelerate or protect cartilage were minimized, and synovial fluid lubricants were not replenished. Thus, the present results and *ex vivo* loading approach provides a baseline to study mechanisms of joint-scale cartilage damage as well as possible interventions.

## 2.6 Acknowledgments

This chapter, in full, was submitted to *The American Journal of Sports Medicine*. The dissertation author was the primary author and thanks co-authors Nasim Eshragh Nia, Alborz Jelvani, Erica G. Gacasan, Aileen Liao, Blair T. Caccam, Albert C. Chen, Koichi Masuda, Robert L. Sah. This work was supported by National Science Foundation Graduate Research Fellowship under Grant No DGE-1144086 (JPC), DOD grant OR13085, and Jack Kent Cooke Graduate Fellowships (NEN, AJ).

## 2.7 References

1. Anderson DD, Chubinskaya S, Guilak F, Martin JA, Oegema TR, Olson SA, Buckwalter JA. Post-traumatic osteoarthritis: Improved understanding and opportunities for early intervention. *J Orthop Res.* 2011;29(6):802-9.
2. Carbone A, Rodeo S. Review of current understanding of post-traumatic osteoarthritis resulting from sports injuries. *J Orthop Res.* 2017;35(3):397-405.
3. Gregory MH, Capito N, Kuroki K, Stoker AM, Cook JL, Sherman SL. A review of translational animal models for knee osteoarthritis. *Arthritis.* 2012;2012:764621.
4. Yoshioka M, Coutts RD, Amiel D, Hacker SA. Characterization of a model of osteoarthritis in the rabbit knee. *Osteoarthritis Cartilage.* 1996;4:87-98.
5. Tochigi Y, Vaseenon T, Heiner AD, Fredericks DC, Martin JA, Rudert MJ, Hillis SL, Brown TD, McKinley TO. Instability dependency of osteoarthritis development in a rabbit model of graded anterior cruciate ligament transection. *J Bone Joint Surg Am.* 2011;93(7):640-7.
6. Sah RL, Yang AS, Chen AC, Hant JJ, Halili RB, Yoshioka M, Amiel D, Coutts RD. Physical properties of rabbit articular cartilage after transection of the anterior cruciate ligament. *J Orthop Res.* 1997;15:197-203.
7. Batiste DL, Kirkley A, Lavery S, Thain LM, Spouge AR, Gati JS, Foster PJ, Holdsworth DW. High-resolution MRI and micro-CT in an ex vivo rabbit anterior cruciate ligament transection model of osteoarthritis. *Osteoarthritis Cartilage.* 2004;12(8):614-26.
8. Batiste DL, Kirkley A, Lavery S, Thain LM, Spouge AR, Holdsworth DW. Ex vivo characterization of articular cartilage and bone lesions in a rabbit ACL transection model of osteoarthritis using MRI and micro-CT. *Osteoarthritis Cartilage.* 2004;12(12):986-96.
9. Kajabi AW, Casula V, Ojanen S, Finnila MA, Herzog W, Saarakkala S, Korhonen RK, Nissi MJ, Nieminen MT. Multiparametric MR imaging reveals early cartilage degeneration at 2 and 8 weeks after ACL transection in a rabbit model. *J Orthop Res.* 2020.
10. Ojanen SP, Finnila MAJ, Makela JTA, Saarela K, Happonen E, Herzog W, Saarakkala S, Korhonen RK. Anterior cruciate ligament transection of rabbits alters composition, structure and biomechanics of articular cartilage and chondrocyte deformation 2weeks post-surgery in a site-specific manner. *J Biomech.* 2020;98:109450.
11. Makela JT, Rezaeian ZS, Mikkonen S, Madden R, Han SK, Jurvelin JS, Herzog W, Korhonen RK. Site-dependent changes in structure and function of lapine articular

- cartilage 4 weeks after anterior cruciate ligament transection. *Osteoarthritis Cartilage*. 2014;22(6):869-78.
12. Roemhildt ML, Coughlin KM, Peura GD, Badger GJ, Churchill D, Fleming BC, Beynnon BD. Effects of increased chronic loading on articular cartilage material properties in the lapine tibio-femoral joint. *J Biomech*. 2010;43(12):2301-8.
  13. Zavatsky AB. A kinematic-freedom analysis of a flexed-knee-stance testing rig. *J Biomech*. 1997;30(3):277-80.
  14. Churchill DL, Incavo SJ, Johnson CC, Beynnon BD. The transepicondylar axis approximates the optimal flexion axis of the knee. *Clin Orthop Relat Res*. 1998;356:111-8.
  15. Maletsky LP, Hillberry BM. Simulating dynamic activities using a five-axis knee simulator. *J Biomech Eng*. 2005;127(1):123-33.
  16. Van Haver A, De Roo K, Claessens T, De Beule M, Verdonk P, De Baets P. Pilot validation study on a quasi-static weight-bearing knee rig. *Proc Inst Mech Eng H*. 2013;227(3):229-33.
  17. Victor J, Van Glabbeek F, Vander Sloten J, Parizel PM, Somville J, Bellemans J. An experimental model for kinematic analysis of the knee. *J Bone Joint Surg Am*. 2009;91 Suppl 6:150-63.
  18. Yildirim G, Walker PS, Boyer J. Total knees designed for normal kinematics evaluated in an up-and-down crouching machine. *J Orthop Res*. 2009;27(8):1022-7.
  19. Forlani F, Sancisi N, Conconi M, Parenti-Castelli V. A new test rig for static and dynamic evaluation of knee motion based on a cable-driven parallel manipulator loading system. *Meccanica*. 2016;51:1571-81.
  20. Levy IM, Torzilli PA, Warren RF. The effect of medial meniscectomy on anterior-posterior motion of the knee. *J Bone Joint Surg Am*. 1982;64-A(6):883-8.
  21. Ballock RT, Woo SL, Lyon RM, Hollis JM, Akeson WH. Use of patellar tendon autograft for anterior cruciate ligament reconstruction in the rabbit: a long-term histologic and biomechanical study. *J Orthop Res*. 1989;7(4):474-85.
  22. Heiner AD, Rudert MJ, McKinley TO, Fredericks DC, Bobst JA, Tochigi Y. In vivo measurement of translational stiffness of rabbit knees. *J Biomech*. 2007;40(10):2313-7.
  23. Mansour JM, Wentorf FA, Degoede KM. In vivo kinematics of the rabbit knee in unstable models of osteoarthrosis. *Ann Biomed Eng*. 1998;26(3):353-60.

24. Gushue D, Houck J, Lerner A. Rabbit knee joint biomechanics: Motion analysis and modeling of forces during hopping. *J Orthop Res.* 2005;23(4):735-42.
25. Grover DM, Chen AA, Hazelwood SJ. Biomechanics of the rabbit knee and ankle: muscle, ligament, and joint contact force predictions. *J Biomech.* 2007;40(12):2816-21.
26. Jadin KD, Wong BL, Bae WC, Li KW, Williamson AK, Schumacher BL, Price JH, Sah RL. Depth-varying density and organization of chondrocyte in immature and mature bovine articular cartilage assessed by 3-D imaging and analysis. *J Histochem Cytochem.* 2005;53(9):1109-19.

## CHAPTER 3

# EX VIVO LOADING OF TRUSSED IMPLANTS FOR SPINE FUSION INDUCES HETEROGENEOUS STRAINS CONSISTENT WITH HOMEOSTATIC BONE MECHANOBIOLOGY

### 3.1 Abstract

A truss structure was recently introduced as an interbody fusion cage. As a truss system, some of the connected elements may be in a state of compression and others in tension. This study aimed to quantify both the mean and variance of strut strains in such an implant when loaded in a simulated fusion condition with vertebral body or contoured plastic loading platens *ex vivo*. Cages were each instrumented with 78 fiducial spheres, loaded between platens (vertebral body or contoured plastic), imaged using high resolution micro-CT, and analyzed for deformation and strain of each of the 221 struts. With repeated loading of a cage by vertebral platens, the distribution (variance, indicated by SD) of strut strains widened from 50N control ( $4 \pm 114 \mu\epsilon$ , mean  $\pm$  SD) to 1000N ( $-23 \pm 273 \mu\epsilon$ ) and 2000N ( $-48 \pm 414 \mu\epsilon$ ), and between 1000N and 2000N. With similar loading of multiple cages, the strain distribution at 2000N ( $23 \pm 389 \mu\epsilon$ ) increased from 50N control. With repeated loading by contoured plastic platens, induced strains at 2000N had a distribution similar to that induced by vertebral platens ( $84 \pm 426 \mu\epsilon$ ). In all studies, cages exhibited increases in strut strain amplitude when loaded from 50N to 1000N or 2000N. Correspondingly, at 2000N, 59-64% of struts exhibited strain amplitudes consistent with mechanobiologically-regulated bone homeostasis. At 2000N, vertically-oriented struts exhibited

deformation of  $-2.87 \pm 2.04 \mu\text{m}$  and strain of  $-199 \pm 133 \mu\epsilon$ , indicating overall cage compression. Thus, using an *ex vivo* 3-D experimental biomechanical analysis method, a truss implant can have strains induced by physiological loading that are heterogeneous and of amplitudes consistent with mechanobiological bone homeostasis.

## 3.2 Introduction

Lumbar spine interbody fusion implants, or cages, are used clinically to induce vertebral fusion as a treatment for degenerative disc disease [1, 2]. These cages provide mechanical support between vertebrae and are typically composed of polyether ether ketone (PEEK) or metal, such as titanium. Many cages are designed for usage with biologics [3-5], such as native or synthetic bone grafts, or growth factors including bone morphogenetic protein (BMP).

Bone formation and remodeling involve mechanobiology, a complex process by which mechanical loads influence the osteogenic biological response [6-10]. With controlled loading *in vitro* or *in vivo*, strain amplitudes up to  $\sim 200\mu\epsilon$  (microstrain,  $10^{-6}$  strain) result in net bone resorption,  $\sim 200$ - $1500\mu\epsilon$  preserve bone homeostasis, and  $>1500\mu\epsilon$  promote bone formation [11-14]. Such mechanobiological strain regimes may be useful to facilitate bone ingrowth into fusion devices [15]. Cage functionality has been described by effects on range of motion *ex vivo*, while clinical effectiveness is evaluated by patient outcome measures and fusion rate [16-17]. Intrinsic cage mechanical function has been assessed experimentally for overall structural properties and theoretically by finite element modeling [17-20]. Local mechanical properties of trabecular bone and other tissues have been quantified *in vitro* [21-24]. However, loading-induced local deformations and strains of spine fusion implants have not previously been quantified.

With the advent of 3-D printing for implants, cages with internal architectures have been introduced. Cages with an open-space trussed architecture may distribute load throughout the cage, allow lateral and axial communication, and provide space for bone growth and fusion [25]. In engineering, truss structures are comprised of linear elements (struts) that are connected at joints (vertices). In response to applied loads, struts are considered to be in either tension (positive) or compression (negative), with a truss in static equilibrium having a sum of forces



equal to zero. Increased loads result in higher magnitude strut forces in both tension (more positive) and compression (more negative), but the net force sum remains zero. We expect that for all the struts in a cage, increased applied load will lead to increased variability of strut deformations/strains (force), with little change to the overall deformation and strain mean ( $\sim$ zero), consistent with a truss structure.

Image-based tracking of intrinsic or affixed markers allows experimental estimation of local strains. More traditional experimental methods elucidate overall implant deformation and strain with platen-to-platen displacement transducers or extensometers, or local strains with mounted strain gauges. These approaches would yield only overall deformation and be difficult to affix to individual and internal struts. Imaging with x-ray or fluoroscopy are often employed to determine the position of spine cages [4, 26]. Such imaging methods, along with image analyses such as texture analysis, can delineate bone deformation *in vitro* to a resolution of  $1.23\mu\text{m}$  and strain of  $300\mu\epsilon$  during physiological loading [27, 28]. With marker-based tracking, high contrast markers are affixed to a structure and the movement of marker positions is assessed with imaging. Such approaches have used extrinsic markers, such as implanted cardiac beads, and intrinsic markers, as with fluorescence microscopy to determine depth-dependent properties of articular cartilage [29, 30]. Such image-based methods could be similarly applied to assess the mechanics of structures such as spine cages.

For orthopaedic biomechanics analysis, 3-D imaging modalities such as  $\mu\text{CT}$ , CT, or MRI have begun to be used [31, 32]. Image analysis of fiducial centroid position typically allows localization at sub-voxel resolution due to the contribution of partial-volume effects at the marker surface [33, 34]. Regional femoral stem micro-motion has been quantified by tracking affixed markers using  $\mu\text{CT}$  [35]. For 3-D printed truss cages, the thin, roughened titanium

material composition facilitates x-ray or ( $\mu$ )CT analysis of internal cage structure. The overall objective of this study was to quantify the local strut-associated strains of cages loaded between vertebral body or contoured plastic platens *ex vivo* after placement of markers, with a particular emphasis on strain distribution, described by both variance and mean.

### 3.3 Methods

#### *Study design.*

For four 4WEB ALIF cages (#1-#4), strut deformation and strain were determined for (1) a single cage (#1) loaded repeatedly with vertebral platens, (2) multiple cages (#2 and #3) loaded with vertebral platens, and (3) a single cage (#4) loaded with contoured plastic platens (**Table 3.1**).

#### *Study 1: Intra-cage Response to Repeated Loading by Vertebral Platens.*

To quantify the distribution of strain between struts, and strain reproducibility, for a given cage loaded with vertebral platens, repeated measures (n=3) of a single cage subjected to 50N, 1000N, and 2000N were made. Strain distribution variance, indicative of increased number of struts in compression (negative) and tension (positive), was compared to 50N control for 1000N and 2000N loads using Levene's tests (median). Comparisons of repeated 50N load vertebral platen control were also made to quantify the sensitivity of strain detection.

#### *Study 2: Inter-Cage Response to Loading by Vertebral Platens.*

Subsequently, to quantify the reproducibility of load-induced strain between cages, two other cages were tested individually, at 50N and 2000N by vertebral platens and compared to 50N control. Strain variance was compared to 50N control at 2000N using Levene's test.

#### *Study 3: Intra-Cage Response to Repeated Loading by Plastic Platens.*

To determine the extent and reproducibility of load-induced strain response to contoured plastic platens, a single cage was loaded repeatedly (n=2) to 50N and 2000N. Strain variance at 2000N was compared with 50N control and that for study 1, 2000N by Levene's tests.

For all studies, strut deformation, strain amplitude, and corresponding percentage of struts exhibiting strains within the combined mechanobiological homeostasis+formation ( $\geq 200\mu\epsilon$ ) ranges were described statistically for each experimental group, and also compared between groups by 1-way ANOVA with *post-hoc* Tukey tests. Also, mean strain was compared with value 0 between all groups. Strut deformation and strain data are reported as mean $\pm$ SD calculated in two ways, by assessing (1) the distribution for struts within each trial/cage (indicated as trial/cage-averaged) to quantify the distribution of deformation and strain internal to individual cages, or (2) the average of all struts within each trial/cage (indicated as strut-averaged) to quantify the variation between trials/cages. In each study, deformation and strain are reported as the distribution, vertical strut distribution, and amplitudes. All groups were tested for normality by the Kolmogorov-Smirnov test. The significance threshold for all statistics was set to  $\alpha=0.05$ . Statistics were performed using Excel (v2013, Microsoft, Redmond, WA, USA) and SPSS (v22, IBM, Armonk, NY, USA).

**Table 3.1:** Study groups for each aim for unloaded and loaded cages with single-cage repeated trials (n) or multiple cages (N).

Study	Platens	Load [N]	n	N
1	vertebral	50	3	1
		1000	3	1
		2000	3	1
2	vertebral	50	1	2
		2000	1	2
3	plastic	50	2	1
		2000	2	1

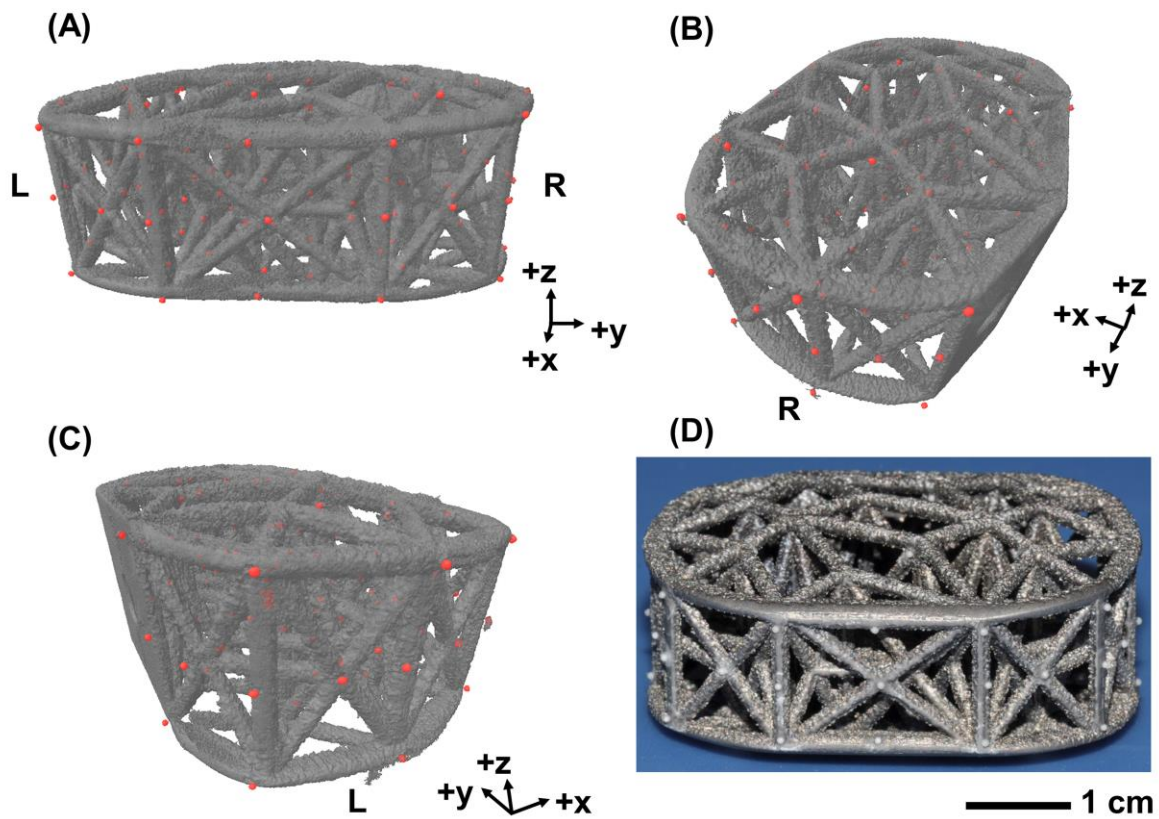
### ***Sample Preparation***

Anterior lumbar interbody fusion (ALIF) cage implants and platens (vertebral body or contoured plastic) were prepared for mechanical loading. ALIF spine implants were provided by 4WEB Medical. The implants had a trussed design (40mm x 27mm x 16mm, LxWxH) with roughened titanium struts (1.25mm diameter). Zirconia spheres (0.5mm diameter) were attached using cyanoacrylate at each vertex (intersection of multiple truss struts) to serve as fiducial markers (66 total) (**Figure 3.1**). Additional spheres (n=12) were placed at the center of some struts, and used to validate the linearity of displacement and thus consistency of strain along a single strut (data not shown). Human vertebral bodies (L4 & L5) from one cadaveric donor (51 year old female) were obtained from a tissue bank (University of Miami) and stored at -80°C. The vertebral bodies were prepared to simulate a fusion condition by excising the L4-L5 intervertebral disc, cutting with an oscillating saw parallel to the endplates and then a rongeur. Plastic platens comprised of polysulfone (an autoclaveable inert plastic) were designed to mimic the vertebral bodies and contoured to provide a counter-surface match to the cages. The prepared vertebral bodies or contoured plastic served as loading platens, superior and inferior to the cage.

### ***Mechanical Loading***

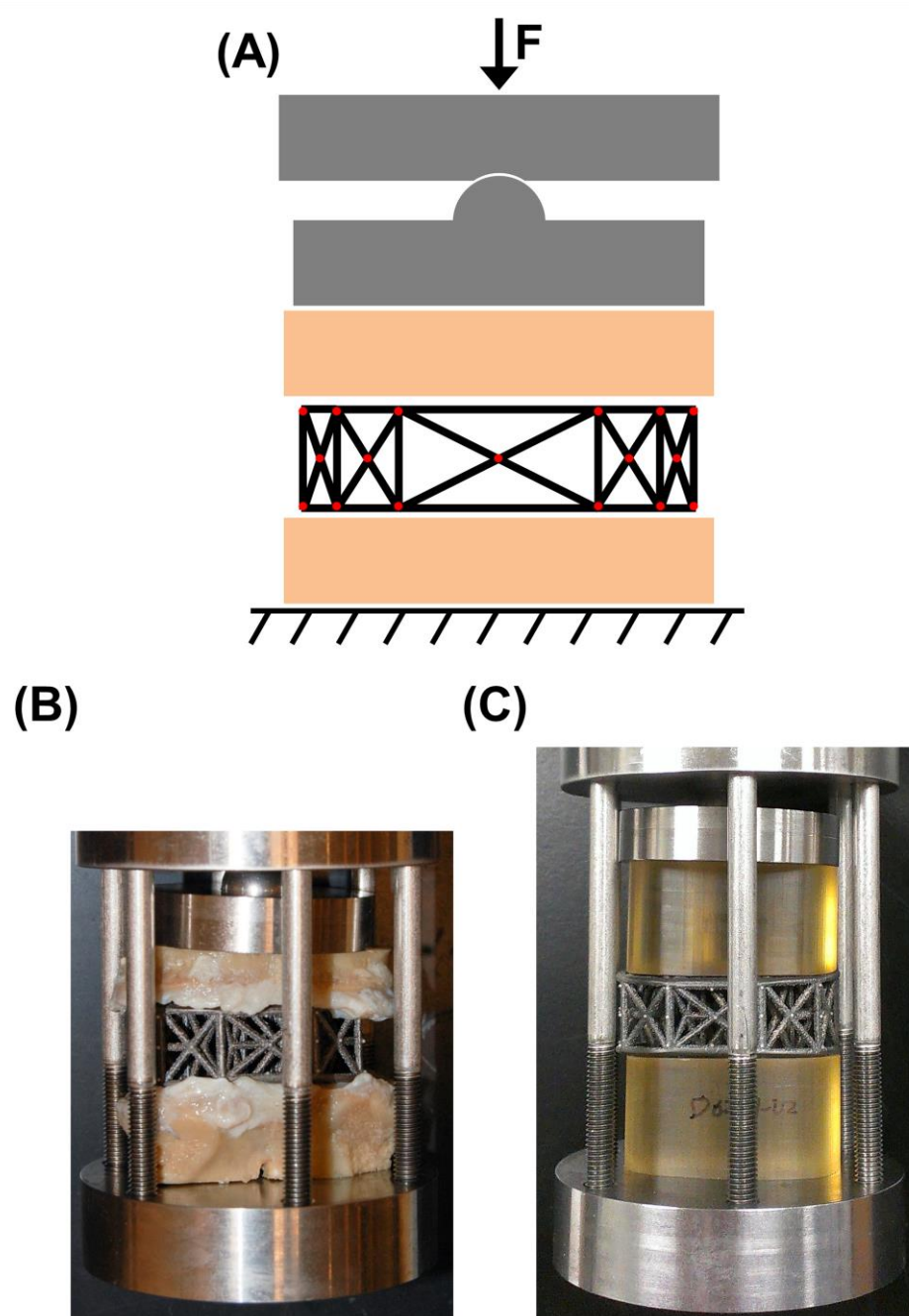
Compressive loads were applied *ex vivo* to cages between loading platens via a custom  $\mu$ CT-compatible compression device with in-line load monitoring. The stand-alone cage was inserted anteriorly without graft material between the vertebral or plastic platens, and the platen-cage-platen complex was loaded. This loading device was designed to fit within a  $\mu$ CT scanner bed and apply compressive loads without interfering with the x-ray transmission paths. A swivel plate allowed for 3 rotational degrees of freedom at one vertebral body to allow the natural

conformation of the platen to the cage (**Figure 3.2**). For samples using donor vertebral body platens, the bone-cage-bone complex was sealed in a fluid-tight bag with phosphate-buffered saline within to maintain high humidity. Compressive loads of 50N, 1000N, or 2000N were applied via the platens to the implant, allowing 10 minutes of relaxation to equilibrium, as determined by the in-line load cell (9000N capacity), prior to imaging. Load levels were selected to represent physiological amplitudes [36, 37]. The 50N load was applied to maintain the cage between the loading platens. Between trials, 30 minutes was allowed for relaxation, during which time, the sample and loading apparatus were disassembled and reassembled.



**Figure 3.1: Structure of 4WEB ALIF cage with affixed fiducial sphere markers.** 3-D microCT volume model of implant (gray) with fiducials attached (red) in (A) posterior, (B) right anterior oblique, and (C) left anterior oblique views. (D) Posterior view photo. Right and Left sides are indicated by “R” and “L”, respectively. Red dots in (A-C) represent attached fiducials.





**Figure 3.2: Cage loading configuration.** (A) Schematic. Photos with (B) vertebral body and (C) plastic platens. Swivel plate allows superior platen to conform to implant lordosis. Arrow indicates direction of force [ $F$ ] application. Red dots in (A) represent attached fiducials.

## ***Imaging & Analysis***

High resolution 3-D images were acquired for each load level and processed to determine location of fiducials. The loaded implant was imaged on a micro-Computed Tomography scanner (Skyscan 1076, Bruker-microCT, Kontich, Belgium) with  $(9\mu\text{m})^3$  voxel size, applying an electrical potential of 100kVp and current of 100uA, using a 0.038mm copper + 0.5mm aluminum filter. A beam-hardening correction algorithm was applied prior to image reconstruction. Images were reconstructed and thresholded (85-255 grayscale values) to segment the radiopaque spheres as fiducials. Image processing included removal of speckles <40000 voxels and Gaussian filtering (radius=10, CTAn, Bruker-microCT, Kontich, Belgium) to remove noise and improve fiducial sphericity and reproducibility. Automated individual object 3-D analysis was performed to calculate fiducial 3-D centroids (CTAn).

Control studies confirmed that a sub-voxel resolution of  $\sim 1\mu\text{m}$  was achieved for detecting load-induced bead displacement. A spring was fitted with radiopaque beads, similar to the cage, with five beads spaced regularly across the length of the spring (38mm), and subjected to 0, 10 $\mu\text{m}$ , and 20 $\mu\text{m}$  of overall compression. After each compression, the sample was imaged by  $\mu\text{CT}$  at  $(9\mu\text{m})^3$  voxel resolution, and bead centroids determined by image processing as described above. For central (N=3) spheres, deviation of the spheres from the predicted position in the x, y, and z image axes were  $0.6\pm 0.4\mu\text{m}$ ,  $0.5\pm 0.3\mu\text{m}$ , and  $1.0\pm 0.5\mu\text{m}$ , respectively, averaged over two trials (mean $\pm$ SD). The variability in each measure represents  $\sim 1/10$  voxel resolution for centroid determination, which is expected due to partial volume effects [38]. Thus for the average strut length of  $\sim 10\text{mm}$ , the z-directed strain resolution was  $1\mu\text{m}/10\text{mm}=100\mu\epsilon$ .

### ***Data Reduction/Calculations***

Deformation, engineering strain, and deformation and strain amplitudes were calculated for each truss strut using pairs of fiducials in an automated fashion using software implemented in MATLAB 2012b (MathWorks, Natick, MA, USA). Fiducial centroids were registered between pairs of scans via 3-D linear transformation (translation and rotation). Using 3-D centroids, struts were automatically defined as pairwise combinations of fiducials, which matched the 221 struts on each cage. A portion of the anterior face of the cage had an instrumentation attachment plate, and connected struts (n=12) were not analyzed. In each of study 1 and the vertebral platen control study, two peripheral fiducials were observed on  $\mu$ CT to make direct contact with the loading platen; thus, the 15 associated struts were excluded from analysis. Strut lengths were calculated for each strut in each trial as the scalar linear distances between sphere pairs in the 50N load conditions ( $9.0 \pm 2.2$ mm, N=221). Deformation was calculated between pairs of scans as the scalar change in length of each strut from 50N initial load to 50N, 1000N, or 2000N final load. Engineering strain (negative in compression, positive in tension) was calculated for each strut as the deformation divided by the initial strut length at 50N. Deformation and strain amplitudes were taken as the absolute values (magnitude) of deformation and strain, respectively. Vertical cage deformation and strain were calculated by averaging values for central axially-oriented struts (N=10).

### 3.4 Results

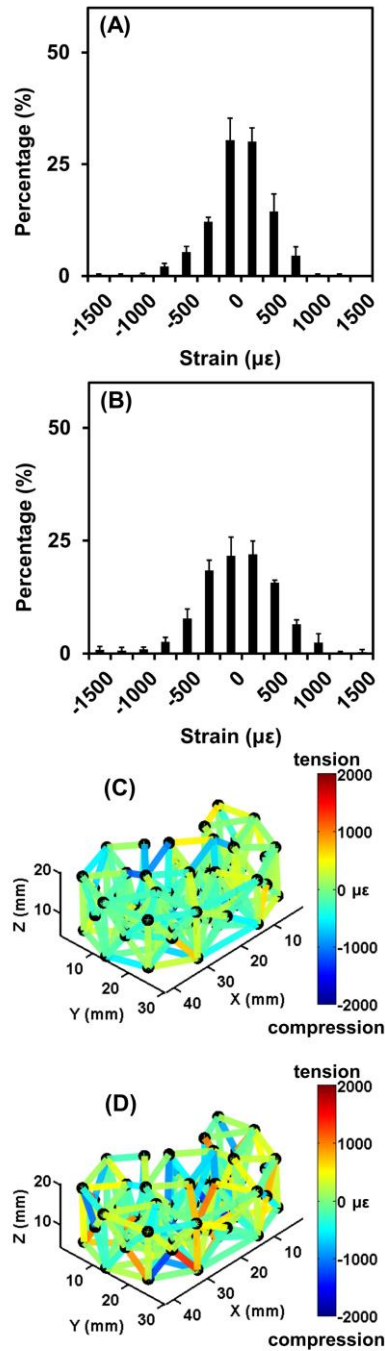
In all studies (described in detail below), cages subjected to 1000N or 2000N load exhibited strut strain distribution variances and amplitudes higher than those of 50N controls. Strain distribution variance for 1000N and 2000N, and amplitude for 2000N, was greater than that of 50N controls in all studies, and those for 2000N were greater than for 1000N in study 1 ( $p < 0.05$ , all pairs). Correspondingly, percentages of strut strain amplitudes in the combined homeostasis+formation ( $\geq 200\mu\epsilon$ ) ranges for 2000N loads were greater than those for 50N controls ( $p < 0.05$ , all pairs). Normality testing on strut-averaged strain showed normally distributed strains for 50N vertebral ( $p = 0.20$ ) and plastic platen ( $p = 0.20$ ) controls, and 2000N groups for studies 1 ( $p = 0.20$ ), 2 ( $p = 0.06$ ), and 3 ( $p = 0.20$ ). Study 1, 1000N and study 3, 2000N trended towards normality ( $p < 0.05$ ). Thus, application of 2000N by either vertebral or plastic platens caused strain distribution to broaden and strain amplitude to increase compared to 50N controls.

#### *Study 1: Intra-cage Response to Repeated Loading by Vertebral Platens.*

##### *Strain Distribution*

In repeated measures of cage #1, physiological loads of 1000N and 2000N, applied with vertebral platens, caused a distribution of strut strains with both positive (tension) and negative (compression) values (**Table 3.2, Figure 3.3**). Trial-averaged ( $n = 3$ ) strain of all struts showed distribution (variance, indicated by SD) that widened from 50N control ( $4 \pm 114\mu\epsilon$ ) to 1000N ( $-23 \pm 273\mu\epsilon$ ) and 2000N ( $-48 \pm 414\mu\epsilon$ ), and between 1000N and 2000N (**Table 3.2**,  $p < 0.05$ , all pairs). Although strain variance increased (larger positive values and more negative values about

the mean), the means of the strain distributions were not different from zero for both 1000N ( $p=0.99$ ) and 2000N ( $p=0.94$ ). Vertical (central axially-oriented struts,  $N=10$ ) strut-averaged deformation was  $0.17\pm 0.60\mu\text{m}$  and  $-1.87\pm 0.82\mu\text{m}$  for 1000N and 2000N load, respectively, and the corresponding vertical strain was  $12\pm 39\mu\epsilon$  and  $-124\pm 52\mu\epsilon$  (**Table 3.3**).



**Figure 3.3: Intra-cage strain distribution for repeated loading by vertebral platens (study 1).** Histograms of strain for all struts in repeated (A) 1000N and (B) 2000N measures. Representative trial strain colormaps for (C) 1000N and (D) 2000N shown on cage layout. Error bars represent SD (n=3). Positive strain values indicate tension and negative strain values indicate compression.

**Table 3.2: Deformation and strain of all struts.** For deformation ( $\Delta L$ ) and strain ( $\epsilon$ ) of struts in each control and loaded group, mean, SDs (variation between trials/cages) of averaged strut values, and SDs (variation between the struts within trial/cage) of average trial/cage values.

Study	Platens	Load [ N ]	Mean		SD, Strut			SD, Trial/Cage		
			$\Delta L$ [ $\mu m$ ]	$\epsilon$ [ $\mu\epsilon$ ]	$\Delta L$ [ $\mu m$ ]	$\epsilon$ [ $\mu\epsilon$ ]	n	$\Delta L$ [ $\mu m$ ]	$\epsilon$ [ $\mu\epsilon$ ]	n
control	vertebral	50	0.04	4	0.96	99	2	0.95	114	206
1	vertebral	1000	-0.19	-23	0.33	35	3	2.29	273	206
1	vertebral	2000	-0.40	-48	0.17	27	3	3.48	414	206
2	vertebral	2000	0.33	23	0.93	107	2	3.45	389	221
control	plastic	50	0.34	38	0.21	25	2	1.12	127	221
3	plastic	2000	0.79	84	0.03	2	2	3.59	426	221

**Table 3.3: Deformation and strain of vertical struts.** For deformation ( $\Delta L$ ) and strain ( $\epsilon$ ) of vertical struts (N=10), mean, SDs of averaged strut values, and SDs of average trial/cage values.

Study	Platens	Load [ N ]	Mean		SD, Strut			SD, Trial/Cage		
			$\Delta L$ [ $\mu m$ ]	$\epsilon$ [ $\mu\epsilon$ ]	$\Delta L$ [ $\mu m$ ]	$\epsilon$ [ $\mu\epsilon$ ]	n	$\Delta L$ [ $\mu m$ ]	$\epsilon$ [ $\mu\epsilon$ ]	n
control	vertebral	50	-0.62	-41	0.19	14	2	0.75	49	206
1	vertebral	1000	0.17	12	0.60	39	3	2.09	148	206
1	vertebral	2000	-1.87	-124	0.82	52	3	3.51	238	206
2	vertebral	2000	-2.87	-199	2.04	133	2	3.80	264	221
control	plastic	50	1.00	66	0.32	20	2	0.44	30	221
3	plastic	2000	-3.30	-224	0.64	41	2	4.30	295	221



### *Strain Amplitude and Mechanobiological Ranges*

Strut-averaged strain amplitude also increased with load, from  $193 \pm 33 \mu\epsilon$  at 50N to  $355 \pm 35 \mu\epsilon$  at 2000N ( $p < 0.05$ ), with that from 50N to 1000N,  $251 \pm 10 \mu\epsilon$ , not reaching significance ( $p = 0.306$ , **Table 3.4**).

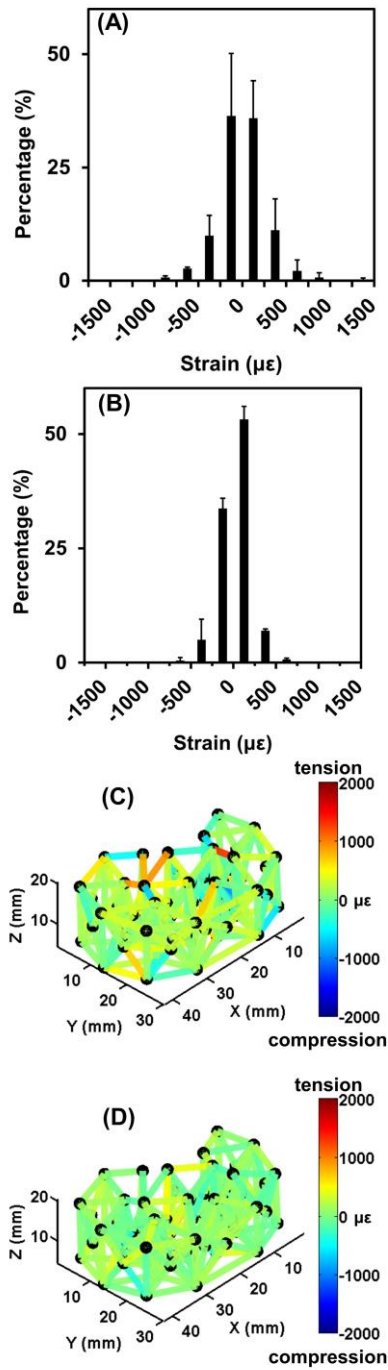
These strain amplitudes corresponded to 49% and 64% homeostasis (200-1500 $\mu\epsilon$ ) and 0% and 1% formation ( $>1500 \mu\epsilon$ ) for 1000N and 2000N load, respectively. Percentages of strut strain amplitudes in the combined homeostasis+formation ( $\geq 200 \mu\epsilon$ ) ranges for 2000N were greater than those for 50N ( $p < 0.05$ ), but not significantly for 1000N ( $p = 0.08$ ).

### *Vertebral Platen Control*

Under repeated 50N tare load, comparison of image datasets yielded strut strain indicative of noise, i.e. relatively small and symmetrically distributed. Repeated trial-averaged ( $n=2$ ) deformation and strain distribution was normally distributed ( $p = 0.20$ , **Figure 3.4A,C**) with small strut-averaged strain amplitudes of  $193 \pm 33 \mu\epsilon$ , respectively (**Table 3.2**), consistent with control loading study, considering the z-direction displacement resolution ( $\sim 100 \mu\epsilon$ ) of two beads. Strain amplitudes corresponded to 37% homeostasis and 0% formation. This baseline measurement for noise indicates that deformation and strain could be assessed with high sensitivity.

**Table 3.4: Amplitudes of deformation and strain of all struts.** For deformation ( $|\Delta L|$ ) and strain ( $|\epsilon|$ ) amplitudes of struts in each control and loaded group, mean, SDs (variation between trials/cages) of averaged strut values, and SDs (variation between the struts within trial/cage) of average trial/cage values.

Study	Platens	Load [ N ]	Mean		SD, Strut		
			$ \Delta L $ [ $\mu\text{m}$ ]	$ \epsilon $ [ $\mu\epsilon$ ]	$ \Delta L $ [ $\mu\text{m}$ ]	$ \epsilon $ [ $\mu\epsilon$ ]	n
control	vertebral	50	1.70	193	0.31	33	2
1	vertebral	1000	2.18	251	0.04	10	3
1	vertebral	2000	3.12	355	0.28	35	3
2	vertebral	2000	2.96	337	0.53	48	2
control	plastic	50	1.16	132	0.11	14	2
3	plastic	2000	2.91	336	0.00	1	2



**Figure 3.4: Intra-cage strain distribution for controls.** Histogram of strain for all struts for (A) vertebral platen and (B) plastic platen controls. Representative trial strain colormaps shown on cage layout for (C) vertebral platen and (D) plastic platen controls. Error bars represent SD ( $n=2$ ). Positive strain values indicate tension and negative strain values indicate compression.

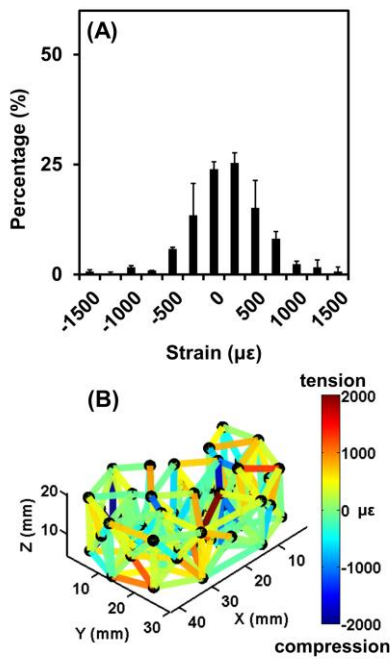
## ***Study 2: Inter-Cage Response to Loading by Vertebral Platens.***

### *Strain Distribution*

The strain distribution at 2000N was similar for two additional cages (#2 and #3, **Table 3.2, Figure 3.5**). Relative to strain distribution at 50N, strain at 2000N,  $23\pm 389\mu\epsilon$ , increased in variance ( $p<0.05$ ) but not in mean ( $p=0.99$ ). Vertical strut-averaged deformation and strain distribution was  $-2.87\pm 2.04\mu\text{m}$  and  $-199\pm 133\mu\epsilon$ , respectively (**Table 3.3**).

### *Strain Amplitude and Mechanobiological Ranges*

Corresponding strut-averaged strain amplitude also increased consistently between cages, from  $193\pm 33\mu\epsilon$  at 50N to  $337\pm 48\mu\epsilon$  at 2000N ( $p<0.05$ , **Table 3.4**). These strain amplitudes corresponded to 59% homeostasis and 1% formation. Percentage of strut strain amplitudes in the combined homeostasis+formation ranges was greater for 2000N than 50N control ( $p<0.05$ ).



**Figure 3.5: Inter-cage strain distribution for loading by vertebral platens (study 2).** (A) Histogram of strain for all struts in multiple cage 2000N measures. (B) Representative cage strain colormap shown on cage layout. Error bars represent SD (N=2). Positive strain values indicate tension and negative strain values indicate compression.

### ***Study 3: Intra-Cage Response to Repeated Loading by Plastic Platens.***

#### *Strain Distribution*

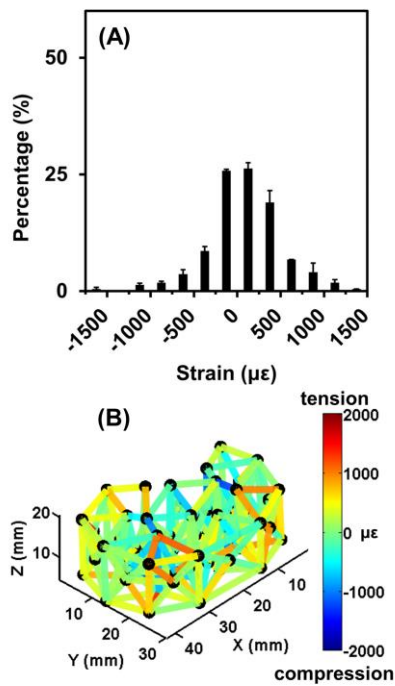
Repeated loading of cage #4 at 2000N with plastic platens induced strains with a distribution similar to those induced by vertebral body platens (**Table 3.2, Figure 3.6**). Trial-averaged (n=2) strain of all struts showed widened distribution (increased variance), from 50N control ( $38\pm 127\mu\epsilon$ ) to 2000N ( $84\pm 426\mu\epsilon$ ,  $p<0.05$ ). Strain variance was similar to that of study 1 for 2000N ( $p=0.92$ ). Also similar to study 1, the means of the strain distributions were not different from zero at 2000N ( $p=0.71$ ). Vertical strut-averaged deformation and strain distribution was  $-3.30\pm 0.64\mu\text{m}$  and  $-224\pm 41\mu\epsilon$ , respectively (**Table 3.3**). Using the vertical strut deformations of the loaded cage (study 3), the apparent stiffness and effective modulus of the cage under axial compression were  $618,000\pm 118,000\text{N/mm}$  and  $12.4\pm 2.4\text{MPa}$ , respectively.

#### *Strain Amplitude and Mechanobiological Ranges*

Strut-averaged strain amplitude also increased with load from 50N control ( $193\pm 33\mu\epsilon$ ) to 2000N ( $336\pm 1\mu\epsilon$ ,  $p<0.05$ , **Table 3.4**). Compared with donor vertebral body platens (study 2, 2000N), strut-averaged strain amplitudes were not significantly different ( $p=0.97$ ). Strain amplitudes corresponded to 59% homeostasis and 0% formation for 2000N load. Percentages of strut strain amplitudes in the combined homeostasis+formation ranges for 2000N were greater than those for 50N control ( $p<0.05$ ). Thus, loading with plastic platens produced strains similar to those induced by loading with vertebral bodies as platens.

### *Plastic Platen Control*

For repeated 50N plastic platen control, trial-averaged (n=2) strain distribution was normally distributed ( $p=0.20$ , **Figure 3.4B,D**) with strut-averaged strain amplitudes of  $132\pm 14\mu\epsilon$ , respectively, similar to vertebral platens ( $p=0.33$ , **Table 3.4**). Corresponding percentages of strain amplitudes in mechanobiological ranges were 21% homeostasis and 0% formation.



**Figure 3.6: Intra-cage strain distribution for repeated loading by plastic platens (study 3).** (A) Histogram of strain for all struts in repeated 2000N measures. (B) Representative trial strain colormap shown on cage layout. Error bars represent SD ( $n=2$ ). Positive strain values indicate tension and negative strain values indicate compression.



### 3.5 Discussion

In the present study, local deformations and strains were quantified for *ex vivo* loaded trussed ALIF cages using  $\mu$ CT to track affixed fiducials. Struts exhibited a strain distribution with approximately equal numbers of struts in compression as tension and centered about zero. Vertical loaded strains, as determined by central axially-oriented struts, showed mainly compressive responses. Repeated compression of a single cage between vertebral platens exhibited deformation and strain amplitudes that increased with physiological load. Loading of multiple cages with vertebral platens indicated comparable strain responses, as did repeated loading with contoured plastic platens.

The study design and approach involved a number of tradeoffs. Cage loading was axial compression, simulating the primary loading applied to the spine; more complex loading conditions, such as bending, torsion, and shear, were not analyzed. Static loading was selected rather than dynamic loading to facilitate imaging and analysis. Strain was calculated as engineering strain from end-to-end strut deformation and length, and assumed to be represent simple compression/tension. Shear, torsion, and bending strains were not assessed.

There was a substantial variation in the deformation of individual struts between trials, although the overall distribution of strut deformation and strain was consistent, with roughly equal number of struts in compression and tension within each trial. Variation between trials for individual struts is likely due to the sensitivity of local strut mechanics to the end-loading conditions of the platens, similar to that recognized for biomechanical testing of trabecular bone [39]. The strain distribution was consistent with a truss in static equilibrium, which has net zero load (some negative, some positive) within the structure. Non-linear overall load-displacement/strain relationships are likely due to complex loading condition between the cage

and platens. The results of the present study extend previous experimental mechanical analysis of interbody fusion cages that address the overall behavior of the vertebral-cage complex or large spine segments [26, 40-42].

The amplitudes of cage strut strains, determined in the present study, are in the range of those mediating mechanobiological homeostasis of bone. Loading up to  $1500\mu\epsilon$  induced a five-fold increase in bone formation in rat tibiae [13]. Induced fluid flow may transduce and amplify the solid strain to higher effective mechanoregulatory signals in the implant [43]. In the post-implant fusion situation, such strain and mechanobiology may be highly relevant to the osteogenic biological response. Bone ingrowth through the cage would likely alter the mechanical environment over time, sharing load transmission with the cage.

The 3-D printed nature of the trussed cages facilitates their design for operation in a targeted mechanobiological response regime. While the present study analyzed and quantified macroscopic strut deformation and strain, microstructural factors may also affect implant performance. Surface roughness, asperities, texture, and charge may modulate local interactions with cells, and subsequent responses, including formation of oriented trabeculae. The similar response of vertebral and contoured plastic platens facilitates future *in vitro* studies of cage mechanobiology, with the latter eliminating the complexity of effects on cage-attached cells of components in post-mortem bone.

In conclusion, the present study provides the first quantification of localized strains throughout a cage structure when subjected to physiological loads. Loaded strut strain amplitudes were largely consistent with mechanobiological homeostasis of bone, which may be an important property for interbody fusion. Further studies are needed to investigate modulation of strain, effective modulus, and mechanobiological cellular response through cage design.

### **3.6 Acknowledgments**

This chapter, in full, was published in *Journal of Biomechanics*. The dissertation author was the primary author and thanks co-authors Esther Cory, Van W. Wong, Koichi Masuda, Albert C. Chen, Jesse P. Hunt, Timothy M. Ganey, and Robert L. Sah. This work was supported by 4WEB Medical (RLS) and the National Science Foundation Graduate Research Fellowship under Grant No DGE-1144086 (JPC).

### 3.7 References

1. Weiner BK, Fraser RD. Lumbar interbody cages. *Spine*. 1998;23(5):634-40.
2. Zdeblick TA, Phillips FM. Interbody cage devices. *Spine*. 2003;28(15 Suppl):S2-7.
3. Bishop RC, Moore KA, Hadley MN. Anterior cervical interbody fusion using autogeneic and allogeneic bone graft substrate: a prospective comparative analysis. *J Neurosurg*. 1996;85(2):206-10.
4. Burkus JK, Gornet MF, Dickman CA, Zdeblick TA. Anterior lumbar interbody fusion using rhBMP-2 with tapered interbody cages. *J Spinal Disord Tech*. 2002;15(5):337-49.
5. Agarwal R, Williams K, Umscheid CA, Welch WC. Osteoinductive bone graft substitutes for lumbar fusion: a systematic review. *J Neurosurg Spine*. 2009;11(6):729-40.
6. Cowin SC, Hegedus DM. Bone remodeling I: A theory of adaptive elasticity. *J Elasticity*. 1976;6:313-25.
7. Turner CH. Three rules for bone adaptation to a mechanical stimuli. *Bone*. 1998;23:399-407.
8. Frost HM. Bone's mechanostat: a 2003 update. *Anat Rec A*. 2003;275(2):1081-101.
9. Mow VC, Huiskes R, editors. *Basic Orthopaedic Biomechanics and Mechano-Biology*. 3rd ed. Philadelphia: Lippincott Williams & Wilkins; 2004.
10. Oftadeh R, Perez-Viloria M, Villa-Camacho JC, Vaziri A, Nazarian A. Biomechanics and mechanobiology of trabecular bone: a review. *Journal of biomechanical engineering*. 2015;137(1):010802.
11. Burger EH, Klein-Nulend J, Veldhuijzen JP. Mechanical stress and osteogenesis in vitro. *J Bone Miner Res*. 1992;7S2:397-401.
12. Akhter MP, Cullen DM, Pedersen EA, Kimmel DB, Recker RR. Bone response to in vivo mechanical loading in two breeds of mice. *Calcif Tissue Int*. 1998;63(5):442-9.
13. Cullen DM, Smith RT, Akhter MP. Bone-loading response varies with strain magnitude and cycle number. *J Appl Physiol*. 2001;91(5):1971-6.
14. Duncan RL, Turner CH. Mechanotransduction and the functional response of bone to mechanical strain. *Calcif Tissue Int*. 1995;57(5):344-58.

15. Reid JJ, Johnson JS, Wang JC. Challenges to bone formation in spinal fusion. *J Biomech.* 2011;44(2):213-20.
16. Burkus JK, Transfeldt EE, Kitchel SH, Watkins RG, Balderston RA. Clinical and radiographic outcomes of anterior lumbar interbody fusion using recombinant human bone morphogenetic protein-2. *Spine.* 2002;27(21):2396-408.
17. Fogel GR, Parikh RD, Ryu SI, Turner AW. Biomechanics of lateral lumbar interbody fusion constructs with lateral and posterior plate fixation: laboratory investigation. *J Neurosurg Spine.* 2014;20(3):291-7.
18. Adam C, Pearcy M, McCombe P. Stress analysis of interbody fusion--finite element modelling of intervertebral implant and vertebral body. *Clin Biomech.* 2003;18(4):265-72.
19. Bevill G, Keaveny TM. Trabecular bone strength predictions using finite element analysis of micro-scale images at limited spatial resolution. *Bone.* 2009;44(4):579-84.
20. Choi KC, Ryu KS, Lee SH, Kim YH, Lee SJ, Park CK. Biomechanical comparison of anterior lumbar interbody fusion: stand-alone interbody cage versus interbody cage with pedicle screw fixation -- a finite element analysis. *BMC Musculoskelet Disord.* 2013;14:220-9.
21. Keaveny TM, Morgan EF, Niebur GL, Yeh OC. Biomechanics of trabecular bone. *Annu Rev Biomed Eng.* 2001;3:307-33.
22. Nagaraja S, Couse TL, Guldborg RE. Trabecular bone microdamage and microstructural stresses under uniaxial compression. *J Biomech.* 2005;38(4):707-16.
23. Suffoletto MS, Dohi K, Cannesson M, Saba S, Gorcsan J, 3rd. Novel speckle-tracking radial strain from routine black-and-white echocardiographic images to quantify dyssynchrony and predict response to cardiac resynchronization therapy. *Circulation.* 2006;113(7):960-8.
24. Muller R. Hierarchical microimaging of bone structure and function. *Nat Rev Rheumatol.* 2009;5(7):373-81.
25. Kiapour A, Vijay G, Ferrara L, Hunt J, editors. Subsidence evaluation of 4-WEB, a novel cross strut based, interbody cage design. International Society for the Study of the Lumbar Spine (ISSLS); 2011; Gothenburg, Sweden.
26. Nayak AN, Gutierrez S, Billys JB, Santoni BG, Castellvi AE. Biomechanics of lateral plate and pedicle screw constructs in lumbar spines instrumented at two levels with laterally placed interbody cages. *Spine J.* 2013;13(10):1331-8.

27. Bay BK, Yerby SA, McLain RF, Toh E. Measurement of strain distributions within vertebral body sections by texture correlation. *Spine*. 1999;24:10-7.
28. Bay BK, Smith TS, Fyhrie DP, Saad M. Digital volume correlation: Three-dimensional strain mapping using X-ray tomography. *Exp Mech*. 1999;39(3):217-26.
29. Schinagl RM, Gurskis D, Chen AC, Sah RL. Depth-dependent confined compression modulus of full-thickness bovine articular cartilage. *J Orthop Res*. 1997;15:499-506.
30. Zerhouni EA, Parish DM, Rogers WJ, Yang A, Shapiro EP. Human heart: tagging with MR imaging--a method for noninvasive assessment of myocardial motion. *Radiology*. 1988;169:59-63.
31. Williams AL, Gornet MF, Burkus JK. CT evaluation of lumbar interbody fusion: current concepts. *Am J Neuroradiol*. 2005;26(8):2057-66.
32. Meisel HJ, Schnoring M, Hohaus C, Minkus Y, Beier A, Ganey T, Mansmann U. Posterior lumbar interbody fusion using rhBMP-2. *Eur Spine J*. 2008;17(12):1735-44.
33. Penney GP, Weese J, Little JA, Desmedt P, Hill DL, Hawkes DJ. A comparison of similarity measures for use in 2-D-3-D medical image registration. *IEEE Trans Med Imaging*. 1998;17(4):586-95.
34. Van Sint Jan S, Salvia P, Hilal I, Sholukha V, Rooze M, Clapworthy G. Registration of 6-DOFs electrogoniometry and CT medical imaging for 3D joint modeling. *J Biomech*. 2002;35(11):1475-84.
35. Gortchacow M, Wettstein M, Pioletti DP, Terrier A. A new technique to measure micromotion distribution around a cementless femoral stem. *J Biomech*. 2011;44(3):557-60.
36. Schultz AB, Andersson GB, Haderspeck K, Ortengren R, Nordin M, Bjork R. Analysis and measurement of lumbar trunk loads in tasks involving bends and twists. *J Biomech*. 1982;15(9):669-75.
37. Nachemson A. Towards a better understanding of low-back pain: a review of the mechanics of the lumbar disc. *Rheumatol Rehabil*. 1975;14(3):129-43.
38. Verhulp E, van Rietbergen B, Huiskes R. A three-dimensional digital image correlation technique for strain measurements in microstructures. *J Biomech*. 2004;37(9):1313-20.
39. Keaveny TM, Pinilla TP, Crawford RP, Kopperdahl DL, Lou A. Systematic and random errors in compression testing of trabecular bone. *J Orthop Res*. 1997;15(1):101-10.

40. Coe JD, Warden KE, Sutterlin CE, 3rd, McAfee PC. Biomechanical evaluation of cervical spinal stabilization methods in a human cadaveric model. *Spine*. 1989;14(10):1122-31.
41. Rapoff AJ, Ghanayem AJ, Zdeblick TA. Biomechanical comparison of posterior lumbar interbody fusion cages. *Spine*. 1997;22(20):2375-9.
42. Wang L, Huang H, Zhang Z, Zhang L, Li J. Biomechanical Evaluation of a Novel Autogenous Bone Interbody Fusion Cage for Posterior Lumbar Interbody Fusion in a Cadaveric Model. *Spine*. 2014;39:E684-92.
43. Zhao F, Vaughan TJ, McNamara LM. Multiscale fluid-structure interaction modelling to determine the mechanical stimulation of bone cells in a tissue engineered scaffold. *Biomechanics and modeling in mechanobiology*. 2015;14(2):231-43.

## CHAPTER 4

### STRAINS IN TRUSSED SPINE INTERBODY FUSION IMPLANTS ARE MODULATED BY LOAD AND DESIGN

#### 4.1 Abstract

Titanium cages with 3-D printed trussed open-space architectures may provide an opportunity to deliver targeted mechanical behavior in spine interbody fusion devices. The ability to control mechanical strain, at levels known to stimulate an osteogenic response, to the fusion site could lead to development of optimized therapeutic implants that improve clinical outcomes. In this study, cages of varying design (1.00mm or 0.75mm diameter struts) were mechanically characterized and compared for multiple compressive load magnitudes in order to determine what impact certain design variables had on localized strain. Each cage was instrumented with small fiducial sphere markers (88 total) at each strut vertex of the truss structure, which comprised of 260 individual struts. Cages were subjected to a 50N control, 1000N, or 2000N compressive load between contoured loading platens in a simulated vertebral fusion condition, during which the cages were imaged using high-resolution micro-CT. The cage was analyzed as a mechanical truss structure, with each strut defined as the connection of two vertex fiducials. The deformation and strain of each strut was determined from 50N control to 1000N or 2000N load by tracking the change in distance between each fiducial marker. As in a truss system, the number of struts in tension (positive strain) and compression (negative strain) were roughly equal, with increased loads resulting in a widened distribution (SD) compared with



that at 50N tare load indicating increased strain magnitudes. Strain distribution increased from 1000N ( $+156\pm 415\mu\epsilon$ ) to 2000N ( $+180\pm 605\mu\epsilon$ ) in 1.00mm cages, which was similar to 0.75mm cages ( $+132\pm 622\mu\epsilon$ ) at 1000N load. Strain amplitudes increased 42%, from  $346\mu\epsilon$  at 1000N to  $492\mu\epsilon$  at 2000N, for 1.00mm cages. At 1000N, strain amplitude in 0.75mm cages ( $481\mu\epsilon$ ) was higher by 39% than that in 1.00mm cages. These amplitudes corresponded to the mechanobiological range of bone homeostasis+formation, with  $63\pm 2\%$  ( $p<0.05$  vs other groups),  $72\pm 3\%$ , and  $73\pm 1\%$  of struts within that range for 1.00mm at 1000N, 1.00mm at 2000N, and 0.75mm at 1000N, respectively. The effective compressive modulus for both cage designs was also dependent on strut diameter, with modulus decreasing from  $12.1\pm 2.3\text{GPa}$  (1.25mm) to  $9.2\pm 7.5\text{GPa}$  (1.00mm) and  $3.8\pm 0.6\text{GPa}$  (0.75mm). This study extended past micro-scale mechanical characterization of trussed cages to compare the effects of design on cage mechanical behavior at moderate (1000N) and strenuous (2000N) load levels. The findings suggest that future cage designs may be modulated to target desired mechanical strain regimes at physiological loads.

## 4.2 Introduction

The load-bearing behavior of spine interbody fusion devices (cages) may dictate the mechanobiological mechanisms by which bone forms. Bone formation and remodeling involve mechanobiology, a complex process by which mechanical loads influence the osteogenic biological response [1-5]. With controlled loading *in vitro* or *in vivo*, strain amplitudes up to  $\sim 200\mu\epsilon$  (microstrain,  $10^{-6}$  strain) result in net bone resorption,  $\sim 200$ - $1500\mu\epsilon$  preserve bone homeostasis, and  $>1500\mu\epsilon$  promote bone formation [6-9]. Bone, including its indwelling cells, is sensitive to tissue strain, induced fluid flow in canaliculi, and induced streaming potentials [10]. For remodeling bone attached to surfaces of a fusion device subjected to compressive and tensile loads, mechanobiological strain regimes may be useful to stimulate bone growth in fusion devices [11,12]. The lack of bone formation within and around a cage may lead to cage subsidence and/or stress shielding after implantation and negatively affect fusion outcome [11,13]. Many orthopaedic devices are designed to minimize the effects of stress shielding, in which low post-implant bone tissue strains lead to resorption [14]. The effective mechanical stiffness and modulus of an implant considers both the material and structure to convey the overall implant behavior under load [15]. By altering cage design, the effective stiffness may be modulated to reduce the effects of stress shielding.

Several different cage designs have been developed for spinal fusion devices, though mechanical characterization has been mostly limited to numerical estimation or overall structural properties. Numerical methods, such as the finite element method, enable estimation of implant stresses and strains under load, but make assumptions in loading, particularly for a complex structure such as a spine cage [16,17]. Experimental mechanical analyses of fusion devices are typically limited to overall structure properties or range of motion measures, using x-ray or

biplane radiography [14,18,19]. However, the mechanics of spine cages can be complex due to cage architecture and the interfaces between cage and loading platen. In addition, with the growth of additive manufacturing, 3-D printed titanium cages with internal architectures have been introduced. One such cage was developed with an open space truss design. This anterior lumbar interbody fusion (ALIF) cage design (4WEB Medical) distributes load throughout the cage, allows lateral and axial communication, and provides space for bone incorporation throughout the implant [20].

Recently, the mechanical properties of struts in a trussed lumbar fusion cage under induced load have been characterized. In that study, a cage design with 1.25mm strut diameter and an anterior instrumentation attachment plate was loaded up to 2000N in repeated measures and for multiple cages with vertebral and contoured plastic loading platens [21]. Spherical fiducials were affixed to vertices of the cage truss struts and tracked by micro-CT during loading to determine individual strut deformations and strains. In that study, struts deformed in a manner statistically dependent on load amplitude, with macroscopic strut strains primarily in the homeostatic range (37% to 64% at 1000N and 2000N loads, respectively) and very few struts in the formation range (0% to 1% at 1000N and 2000N, respectively). As the number of struts in the homeostatic and formation strain ranges may be an important factor for implant bone ingrowth, study of similar cage designs with thinner, and thus more compliant, struts was warranted. Thus, the objective of this study was to extend the previous studies and quantify and compare the strut strains for a trussed cage design with thinner (0.75mm or 1.00mm) struts and no instrumentation attachment plate, and to assess what the effect of these designs would have on strut strain levels, in particular, the range predicted to affect bone mechanobiology.

### 4.3 Materials and Methods

#### *Study Design*

This overview of the experimental and analysis approach describes the measures and statistical comparisons used in the study. Strut deformation and strain were determined for multiple cages (n=2) for truss strut diameters of 1.00mm or 0.75mm (**Table 4.1**). Cages were loaded by contoured plastic platens to 50N or 1000N for 0.75mm strut diameter and 50N, 1000N, or 2000N for 1.00mm strut diameter. Loads of 1000N and 2000N were selected to represent physiological lumbar load amplitudes of moderate and strenuous activities, respectively [22,23]. Strain distribution variance, indicative of strut amplitudes in either compression (negative) and tension (positive), was compared for 1000N and 2000N loads using Levene's tests (median). (Levene's tests were used to directly compare variance between groups, which other statistical tests, such as ANOVA, assumed to be equal between groups.) Strut strain amplitude and corresponding percentage of struts exhibiting strains within the combined mechanobiological homeostasis+formation ( $\geq 200\mu\epsilon$ ) ranges were described statistically for each group to show the effect of loading and cage design on potential mechanobiological osteogenic effects. Strut-averaged strain amplitudes (mean of all struts for each cage) and homeostasis+formation percentages were compared between groups by 1-way ANOVA with *post-hoc* Tukey tests. Mean strain was compared with value 0 between all groups for vertically oriented struts to show overall implant axial behavior; in contrast, as a control analysis, the mean strain in all struts was compared to an unloaded mechanical truss (which exhibits net zero strains by definition) and thus was not expected to show a difference. Strut deformation and strain data are reported as mean $\pm$ SD calculated in two ways, by assessing (1) the distribution within cages

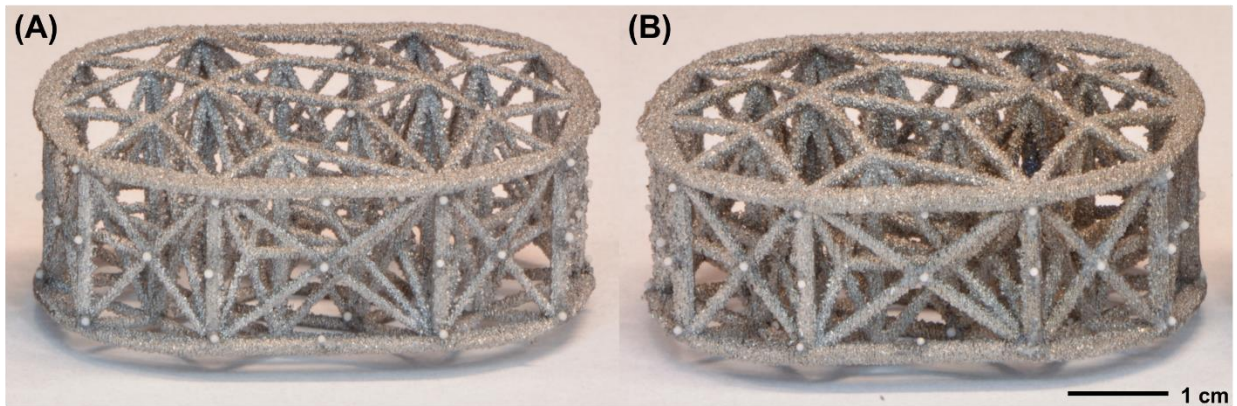
(indicated as cage-averaged) to quantify the distribution of deformation and strain internal to individual cages, or (2) the average of all struts within each cage (indicated as strut-averaged) to quantify the variation between cages. In each study, deformation and strain are reported as the distribution, vertical strut distribution, and amplitudes. Groups were tested for normality by the Kolmogorov-Smirnov test. Sample size was selected based on previous study effective modulus ( $12.1 \pm 2.3$  GPa) and 46% projected modulus reduction (strut cross-sectional area change with diameter decrease from 1.25mm to 1.00mm) with power of 80%. The significance threshold for all statistics was set to  $\alpha=0.05$ . Statistics were performed using Excel (v2013, Microsoft, Redmond, WA, USA) and SPSS (v23, IBM, Armonk, NY, USA).

**Table 4.1:** Study groups for 1.00mm and 0.75mm cages loaded at 50N, 1000N, or 2000N.

<b>Study</b>	<b>Strut Diameter [mm]</b>	<b>Load [N]</b>	<b>N</b>
1	0.75	50	2
		1000	2
2	1.00	50	2
		1000	2
		2000	2

### *Cage Preparation*

Cage implants, similar to those studied previously, but with thinner struts and no instrumentation attachment plate, were provided by 4WEB Medical. Contoured polysulfone (an autoclaveable inert plastic; elastic modulus 2.5GPa) platens that were designed to conform to the biconvex surface of the cage were used to allow distributed compressive loading. Contour match was achieved by designing platens surface curvature to match that of a representative cage, based on  $\mu$ CT imaging. The implants had a trussed design (40mm x 27mm x 16mm, LxWxH) and biconvex contour on the top (superior) and bottom (inferior) faces with roughened titanium struts (0.75mm or 1.00mm diameter, **Fig. 4.1**). Zirconia spheres (0.5mm diameter) were attached using cyanoacrylate at each vertex (intersection of multiple truss struts) to serve as fiducial markers (88 total).



**Figure 4.1: Design of trussed cages with affixed fiducial markers.** Photos of cages with (A) 0.75mm and (B) 1.00mm strut diameter from posterior view.



### ***Mechanical Loading***

Compressive loads were applied to cages between the loading platens via a custom  $\mu$ CT-compatible compression device with in-line load monitoring, as described previously [21]. Briefly, the stand-alone cage was inserted without graft material between the platens, and the platen-cage-platen complex was loaded. This loading device was designed to fit within a  $\mu$ CT scanner bed and apply compressive loads without interfering with the x-ray transmission paths. A swivel plate allowed for 3 rotational degrees of freedom at one vertebral body to allow the natural conformation of the platen to the cage. Compressive loads of 50N, 1000N, or 2000N were applied via the platens to the implant. The 50N load was applied to maintain the cage between the loading platens.

### ***Imaging & Data Analysis***

Imaging by  $\mu$ CT and subsequent analysis to track bead centroids at each load level were performed by automated quantitative image analysis. Cages were imaged in 3-D using  $\mu$ CT with  $(9\mu\text{m})^3$  voxel size. Images were reconstructed, thresholded (85-255 grayscale values), speckles removed ( $<40,000$  voxels), and smoothed (Gaussian filtering, radius= 10, CTAn, Bruker-microCT, Kontich, Belgium) to segment the radiopaque spheres as fiducial markers. Object analysis was performed to determine fiducial 3-D centroids for each of the 88 fiducials (CTAn). Fiducials from each scan series were co-registered via linear transformation to align scans and account for any shifting between scans. The lengths of each of the 260 cage struts were determined as the distance between appropriate pairs of centroids, and the change in length from 50N load taken to be deformation; deformation relative to the original length in the 50N state was taken to be engineering strain (negative in compression, positive in tension). For each study,

deformation and strain were reported both as signed distributions (positive and negative values) and as absolute values (magnitude). Previous control studies showed that sub-voxel resolution of  $\sim 1\mu\text{m}$  was achieved for detecting load-induced bead displacement [21]. For the average strut length of  $\sim 10\text{mm}$ , the resolution was  $1\mu\text{m}/10\text{mm}=100\mu\epsilon$ .

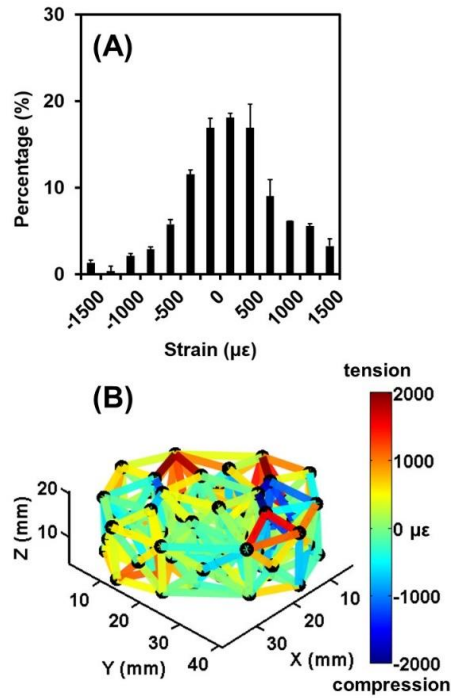
Vertical cage struts were also analyzed separately to represent overall implant axial behavior. Vertical cage deformation and strain were defined as the subset of central axially-oriented struts ( $N=10$ ). The central region of axially-oriented struts was selected, excluding peripheral axially-oriented struts, to avoid possible abnormal loading due to edge effects or limited interface with platens.

The effective implant stiffness and modulus was estimated for both implant designs (0.75mm, 1.00mm) using the average of strut deformation and strain of the struts that were vertically-oriented (aligned with loading axis). Effective moduli were compared to that of 1.25mm cages studied previously [21]. For the 1.00mm cages at 2000N load and 0.75mm cages at 1000N load, the vertical strut deformation was normalized by load to yield stiffness. Effective modulus was determined by normalizing stiffness to height and the overall implant footprint area ( $\sim 800\text{mm}^2$ ). The stiffness and effective modulus represent the overall implant mechanical behavior in axial compression, relative to an object of the same footprint cross-sectional area.

## 4.4 Results

### *Strain Distribution*

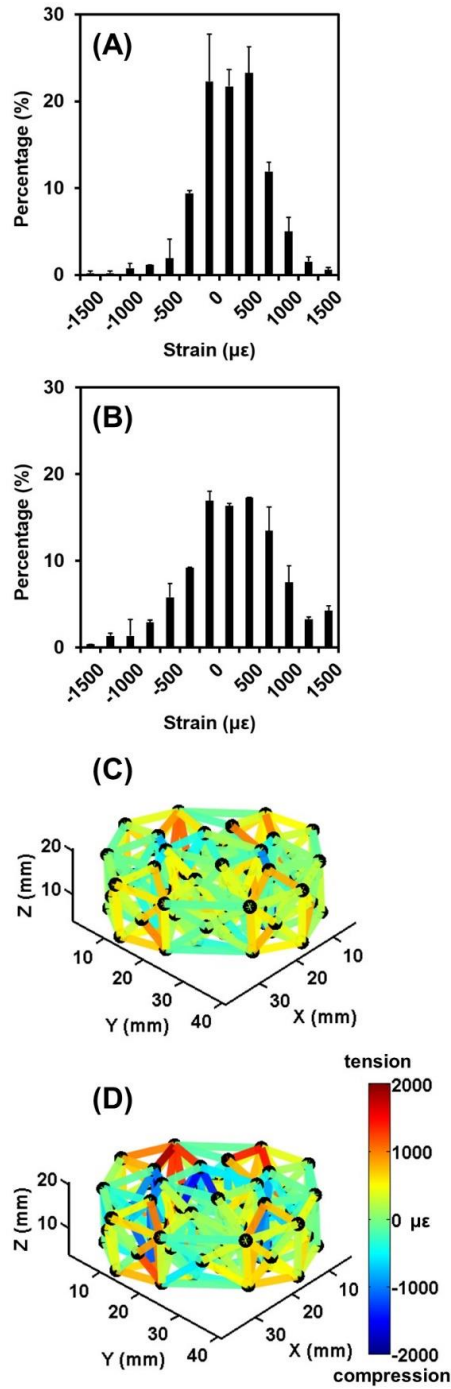
For each cage, loading to 1000N or 2000N caused a distribution of strut deformations and strains, with both positive (tension) and negative (compression) values (**Fig. 4.2, Table 4.2**). For 0.75mm cages loaded to 1000N, struts exhibited an overall strain distribution that had a positive mean ( $+132\pm 622\mu\epsilon$ ,  $n=260$ ,  $p<0.05$ , **Fig. 4.2A,B**), whereas the vertical struts exhibited a negative mean strain ( $-346\pm 379\mu\epsilon$ ,  $n=10$ ,  $p<0.05$ , **Table 4.3**). In 1.00mm cages, struts exhibited a widened strain distribution (variance  $p<0.05$ , **Fig. 4.3A-D**) as load increased from 1000N ( $+156\pm 415\mu\epsilon$ ,  $n=260$ ,  $p<0.05$ ) to 2000N ( $+180\pm 605\mu\epsilon$ ,  $n=260$ ,  $p<0.05$ ), while vertical struts exhibited strain at 1000N that was indistinguishable from zero ( $-5\pm 314\mu\epsilon$ ,  $n=10$ ,  $p=0.96$ ), and trended toward decreasing at 2000N ( $-288\pm 508\mu\epsilon$ ,  $n=10$ ,  $p=0.10$ ). Normality testing on strut-averaged strain showed strains that were distributed normally for 1000N ( $p=0.20$ ) and 2000N ( $p=0.20$ ) for the 1.00mm group, and near normal for 1000N ( $p=0.03$ ) in the 0.75mm group



**Figure 4.2: Strain distribution for 0.75mm cages.** Histogram of strain for all struts in 0.75mm cages at (A) 1000N. Representative cage strain colormaps for 0.75mm cages at (B) 1000N shown on cage layout. Error bars represent SD (n=2). Positive strain values indicate tension and negative strain values indicate compression.

**Table 4.2: Deformation and strain of all struts.** For deformation ( $\Delta L$ ) and strain ( $\epsilon$ ) of struts in each group, mean, SDs (variation between cages) of averaged strut values (SD, Strut), and SDs (variation between the struts within cage) of average cage values (SD, Cage).

Study	Strut Diameter [ mm ]	Load [ N ]	Mean		SD, Strut			SD, Cage		
			$\Delta L$ [ $\mu m$ ]	$\epsilon$ [ $\mu\epsilon$ ]	$\Delta L$ [ $\mu m$ ]	$\epsilon$ [ $\mu\epsilon$ ]	n	$\Delta L$ [ $\mu m$ ]	$\epsilon$ [ $\mu\epsilon$ ]	n
1	0.75	1000	1.26	132	0.23	22	2	5.44	622	260
2	1.00	1000	1.45	156	0.68	71	2	3.56	415	260
2	1.00	2000	1.60	180	0.83	90	2	5.36	605	260



**Figure 4.3: Strain distribution for 1.00mm cages.** Histograms of strain for all struts in 1.00mm cages at (A) 1000N and (B) 2000N load. Representative cage strain colormaps for 1.00mm cages at (C) 1000N and (D) 2000N shown on cage layout. Error bars represent SD (n=2). Positive strain values indicate tension and negative strain values indicate compression.

**Table 4.3: Deformation and strain of vertical struts.** For deformation ( $\Delta L$ ) and strain ( $\epsilon$ ) of vertical struts (N=10), mean, SDs of averaged strut values (SD, Strut), and SDs of average cage values.

Study	Strut Diameter [ mm ]	Load [ N ]	Mean		SD, Strut			SD, Cage		
			$\Delta L$ [ $\mu m$ ]	$\epsilon$ [ $\mu\epsilon$ ]	$\Delta L$ [ $\mu m$ ]	$\epsilon$ [ $\mu\epsilon$ ]	n	$\Delta L$ [ $\mu m$ ]	$\epsilon$ [ $\mu\epsilon$ ]	n
1	0.75	1000	-5.22	-346	0.84	52	2	5.72	379	10
2	1.00	1000	-0.04	-5	1.45	90	2	4.90	314	10
2	1.00	2000	-4.34	-288	3.55	240	2	7.87	508	10

### ***Strain Amplitude and Mechanobiological Ranges***

The amplitude of deformation and strain (averaged for all struts within each cage) exhibited a high reproducibility amongst cages tested under the same conditions (**Table 4.4**) and varied significantly between the two types of cages and the two loading conditions. For 1.00mm cages, average strain amplitude increased 42% ( $p<0.05$ ), from  $346\mu\epsilon$  at 1000N to  $492\mu\epsilon$  at 2000N. Also, at 1000N, average strain amplitude in 0.75mm cages ( $481\mu\epsilon$ ) was higher by 39% ( $p<0.05$ ) than that in 1.00mm cages. For these cages and test conditions, 1.00mm at 1000N, 1.00mm at 2000N, and 0.75mm at 1000N, the percentage of struts in the mechanobiological ranges of homeostasis+formation varied correspondingly,  $63\pm 2\%$  ( $p<0.05$  vs other groups),  $72\pm 3\%$ , and  $73\pm 1\%$ , respectively.

### ***Effective Mechanical Properties***

The effective compressive modulus for both cage types was dependent on strut diameter, with modulus decreasing with strut diameter. For 1.00mm and 0.75mm cages, effective stiffness was  $460\pm 377\text{kN/mm}$  and  $192\pm 31\text{kN/mm}$ , respectively. Normalizing to height and overall cross-sectional area, the effective modulus was  $9.2\pm 7.5\text{GPa}$  and  $3.8\pm 0.6\text{GPa}$  for 1.00mm cage at 2000N load and 0.75mm cage at 1000N load, respectively. The 1.00mm cage at 1000N load had an effective modulus of  $19.6\pm 27.9\text{GPa}$ . For comparison, the 1.25mm cage had an effective modulus of  $12.1\pm 2.3\text{GPa}$  [21].



**Table 4.4: Amplitudes of deformation and strain of all struts.** For deformation ( $|\Delta L|$ ) and strain ( $|\epsilon|$ ) amplitudes of struts in each group, mean, SDs (variation between cages) of averaged strut values (SD, Strut).

Study	Strut Diameter [ mm ]	Load [ N ]	Mean		SD, Strut		
			$ \Delta L $ [ $\mu\text{m}$ ]	$ \epsilon $ [ $\mu\epsilon$ ]	$ \Delta L $ [ $\mu\text{m}$ ]	$ \epsilon $ [ $\mu\epsilon$ ]	n
1	0.75	1000	4.25	481	0.12	14	2
2	1.00	1000	3.04	346	0.15	18	2
2	1.00	2000	4.36	492	0.07	9	2

## 4.5 Discussion

In this study, the mechanical response of trussed fusion cages was modulated by design (strut diameter), as well as load magnitude. The effect of increased strut diameter and increased load (1.00mm at 2000N vs. 0.75mm at 1000N) were found to be counteracting, with roughly the same effect size. Vertical loaded strains, as determined by central axially-oriented struts, showed compressive responses. The effective cage mechanical properties were similarly modulated by strut diameter.

The study involved some limitations. Cage loading was axial compression, simulating the primary loading applied to the spine. The experimental setup mimicked aspects of the *in vivo* loading environment, including platens contoured to cage implants and a swivel plate to allow rotational freedom for natural alignment during loading [21]. While the scenario is a simplified loading condition, it allows for high-resolution mechanical characterization. More complex loading conditions, such as bending, torsion, and shear, were not analyzed. In addition, more complex interfaces between implant and vertebral bone were not analyzed. Strain was calculated as engineering strain from end-to-end strut deformation and length, and assumed to represent simple compression/tension. Only one or two non-zero loads were applied, and thus linearity was not formally assessed.

The deformation and strain of individual struts varied between cages, although the overall distribution of strut deformation and strain was consistent within each group, with roughly equal number of struts in compression and tension within each cage. Variation between cages for individual struts is likely due to the sensitivity of local strut mechanics to the end-loading conditions of the platens, similar to that recognized for biomechanical testing of trabecular bone [24]. The induction of both negative and positive strains with means close to zero within the

trusses of the cages tested is consistent with a truss structure, whereby loads are supported by struts in both compression and tension with net zero strains. This implies that the cage may behave similarly to a truss structure. Load patterns are variable at low loads, particularly for the stiffer 1.00mm cage. This is likely due to irregular roughened surface asperities interfacing with the plastic platens and variability in the precise loading interface conditions between trials. This is unlikely due to plastic deformation since the yield strain of Ti-6Al-4V is ~1% [25], and strain magnitudes of individual vertical struts were less than  $1200\mu\epsilon$  (0.12%) across all groups and trials.

Alteration of strut diameter for cages of similar architecture and size can modulate the deformation and strain response, as well as the effective stiffness and modulus under load. By changing the strut diameter of a cage from 1.00mm to 0.75mm, higher strain amplitudes under load were realized. Increasing applied load by 1000N and decreasing strut diameter by 0.25mm had similar effect sizes. The strut diameters used in this study represent potential designs for trussed cages. Nevertheless, by comparison, thinning of strut diameter from 1.25mm to 1.00mm and 0.75mm decreased stiffness from  $606\pm 116\text{kN/mm}$  to  $460\pm 377\text{kN/mm}$  and  $192\pm 31\text{kN/mm}$ , and from an effective modulus of  $12.1\pm 2.3\text{GPa}$  to  $9.2\pm 7.5\text{GPa}$  (-24%) and  $3.8\pm 0.6\text{GPa}$  (-68%), respectively. The stiffness and effective modulus did not linearly decrease with either strut diameter ( $p=0.11$ ), strut cross-sectional area ( $p=0.15$ ), or  $(\text{strut cross-sectional area})^2$  ( $p=0.24$ ). This suggests that stiffnesses and effective moduli determined in this study do not scale proportionally with strut diameter across cage designs. These effective modulus values are roughly that of healthy vertebral trabecular bone (~2-8GPa, [26]). Thus, the overall structure may minimize endplate stress risers at the cage interface, and provide a dynamic environment to the contained bone graft that mimics the intra-trabecular environment of the vertebrae. This is of

particular importance, as bone is better suited to resist compressive loading predominantly experienced after interbody fusion. It can be compared to an equivalent geometry of titanium, which has an elastic modulus of 118GPa, indicating the higher compliance of the trussed cage designs. We did not include formal statistical comparison to previous studies with 1.25mm struts [179], as those cages contained an anterior face instrumentation attachment plate, whereas the cages used in this study did not. It is speculated that this instrumentation interface may act as a stiffening plate and carry a portion of the load through the cage, which may motivate cage design changes.

The present results extend past studies, in which only ~60% of struts were in the homeostasis+formation range for 1.25mm strut diameter cages subjected to similar loads [21]. In the present study, ~70% of struts exhibited strain amplitudes consistent with mechanically-induced mechanobiological homeostasis (200-1500 $\mu\epsilon$ ), whereas a small percentage (~3%) were consistent with formation (>1500 $\mu\epsilon$ ) [9, 2]. Whereas the majority of struts were found to be in the bone homeostasis and formation strain regime, there was large variability between cages for any single strut. With more complex, dynamic loading *in vivo*, it is reasonable that a wider range of struts would experience strains in the homeostasis and formation regimes with variable duty cycles. The variation of struts in osteogenic strain range with cage design at physiological load levels (1000N, 2000N) suggests that implant structures can be targeted to operate in a desired mechanobiological response regime.

The way in which mechanics of a trussed cage links to bone mechanobiology in a fusion situation has yet to be determined spatially and temporally. The interfaces between the cage and bone may include load-bearing surfaces and those within the cage volume, with or without graft particulates. If bone attaches to the cage struts, strut strains will extend to the bone tissue,

depending on geometries and material properties, including those of the interface. Induced osteocyte signaling for bone deposition may occur from such mechanical strain on affixed bone, or by early remodeling graft tissue. Bone tissue at these interfaces may be responsive to strain-induced fluid flows, in addition to compressive and tensile matrix strains. In addition to strain amplitudes, strain types, such as compression, tension, or shear, likely result in varying cell responses [27]. Induced fluid flow may transduce and amplify the solid strain to higher effective mechanoregulatory signals in the implant [12]. In the post-implant fusion situation, such strain and mechanobiology may be highly relevant to the osteogenic biological response. Bone ingrowth through the cage would likely alter the mechanical environment over time, sharing load transmission with the cage.

Mapping of load-induced strain within interbody fusion cages is a new technical innovation that may aid in improving future designs. The test method allowed analysis of the implant without disturbing its mechanical integrity, and with higher resolution than other current techniques. It did not attempt to measure cell-scale strains, which may be critical for mechanobiological responses. Using this strain-mapping methodology, cages designed with thinner (0.75mm and 1.00mm, instead of 1.25mm diameter) struts resulted in higher percentages of struts in homeostasis and formation ranges under moderate (1000N) and strenuous (2000N) axial compressive loads. This may subsequently improve implant bone ingrowth and overall fusion success.

## 4.6 Acknowledgments

This chapter, in full, was published in *Journal of the Mechanical Behavior of Biomedical Materials*. The dissertation author was the primary author and thanks co-authors Eloy Alonso, Koichi Masuda, Jesse P. Hunt, Cameron N. Carmody, Timothy M. Ganey, and Robert L. Sah. This work was supported by 4WEB Medical (RLS) and the National Science Foundation Graduate Research Fellowship under Grant No DGE-1144086 (JPC).

We would like to thank Albert C. Chen for his assistance in initial study design, and Esther Cory and Van W. Wong for helping establish data collection techniques.

## 4.7 References

1. Cowin SC, Hegedus DM. Bone remodeling I: A theory of adaptive elasticity. *J Elasticity*. 1976;6:313-25.
2. Frost HM. Bone's mechanostat: a 2003 update. *Anat Rec A*. 2003;275(2):1081-101.
3. Mow VC, Huiskes R, editors. *Basic Orthopaedic Biomechanics and Mechano-Biology*. 3rd ed. Philadelphia: Lippincott Williams & Wilkins; 2004.
4. Oftadeh R, Perez-Viloria M, Villa-Camacho JC, Vaziri A, Nazarian A. Biomechanics and mechanobiology of trabecular bone: a review. *Journal of biomechanical engineering*. 2015;137(1):010802.
5. Turner CH. Three rules for bone adaptation to a mechanical stimuli. *Bone*. 1998;23:399-407.
6. Akhter MP, Cullen DM, Pedersen EA, Kimmel DB, Recker RR. Bone response to in vivo mechanical loading in two breeds of mice. *Calcif Tissue Int*. 1998;63(5):442-9.
7. Burger EH, Klein-Nulend J, Veldhuijzen JP. Mechanical stress and osteogenesis in vitro. *J Bone Miner Res*. 1992;7S2:397-401.
8. Cullen DM, Smith RT, Akhter MP. Bone-loading response varies with strain magnitude and cycle number. *J Appl Physiol*. 2001;91(5):1971-6.
9. Duncan RL, Turner CH. Mechanotransduction and the functional response of bone to mechanical strain. *Calcif Tissue Int*. 1995;57(5):344-58.
10. Dallas SL, Prideaux M, Bonewald LF. The osteocyte: an endocrine cell ... and more. *Endocrine reviews*. 2013;34(5):658-90.
11. Reid JJ, Johnson JS, Wang JC. Challenges to bone formation in spinal fusion. *J Biomech*. 2011;44(2):213-20.
12. Zhao F, Vaughan TJ, McNamara LM. Multiscale fluid-structure interaction modelling to determine the mechanical stimulation of bone cells in a tissue engineered scaffold. *Biomech Model Mechanobiol*. 2015;14(2):231-43.
13. Blumenthal SL, Ohnmeiss DD. Intervertebral cages for degenerative spinal diseases. *Spine J*. 2003;3(4):301-9.

14. Kanayama M, Cunningham BW, Haggerty CJ, Abumi K, Kaneda K, McAfee PC. In vitro biomechanical investigation of the stability and stress-shielding effect of lumbar interbody fusion devices. *J Neurosurg.* 2000;93(2 Suppl):259-65.
15. Parthasarathy J, Starly B, Raman S, Christensen A. Mechanical evaluation of porous titanium (Ti6Al4V) structures with electron beam melting (EBM). *J Mech Behav Biomed Mater.* 2010;3(3):249-59.
16. Fan CY, Hsu CC, Chao CK, Lin SC, Chao KH. Biomechanical comparisons of different posterior instrumentation constructs after two-level ALIF: a finite element study. *Med Eng Phys.* 2010;32(2):203-11.
17. Xu H, Tang H, Guan X, Jiang F, Xu N, Ju W, Zhu X, Zhang X, Zhang Q, Li M. Biomechanical comparison of posterior lumbar interbody fusion and transforaminal lumbar interbody fusion by finite element analysis. *Neurosurgery.* 2013;72(1 Suppl Operative):21-6.
18. Fogel GR, Parikh RD, Ryu SI, Turner AW. Biomechanics of lateral lumbar interbody fusion constructs with lateral and posterior plate fixation: laboratory investigation. *J Neurosurg Spine.* 2014;20(3):291-7.
19. Nayak AN, Gutierrez S, Billys JB, Santoni BG, Castellvi AE. Biomechanics of lateral plate and pedicle screw constructs in lumbar spines instrumented at two levels with laterally placed interbody cages. *Spine J.* 2013;13(10):1331-8.
20. Kiapour A, Vijay G, Ferrara L, Hunt J, editors. Subsidence evaluation of 4-WEB, a novel cross strut based, interbody cage design. International Society for the Study of the Lumbar Spine (ISSLS); 2011; Gothenburg, Sweden.
21. Caffrey JP, Cory E, Wong VW, Masuda K, Chen AC, Hunt JP, Ganey TM, Sah RL. Ex vivo loading of trussed implants for spine fusion induces heterogeneous strains consistent with homeostatic bone mechanobiology. *J Biomech.* 2016;49:4090-7.
22. Nachemson A. Towards a better understanding of low-back pain: a review of the mechanics of the lumbar disc. *Rheumatol Rehabil.* 1975;14(3):129-43.
23. Schultz AB, Andersson GB, Haderspeck K, Ortengren R, Nordin M, Bjork R. Analysis and measurement of lumbar trunk loads in tasks involving bends and twists. *J Biomech.* 1982;15(9):669-75.
24. Keaveny TM, Pinilla TP, Crawford RP, Kopperdahl DL, Lou A. Systematic and random errors in compression testing of trabecular bone. *J Orthop Res.* 1997;15(1):101-10.
25. Khan AS, Kazmi R, Farrokh B. Multiaxial and non-proportional loading responses, anisotropy and modeling of Ti-6Al-4V titanium alloy over wide ranges of strain rates and temperatures. *Int J Plasticity.* 2007;23:931-50.



26. Keaveny TM, Morgan EF, Niebur GL, Yeh OC. Biomechanics of trabecular bone. *Annu Rev Biomed Eng.* 2001;3:307-33.
27. Klein-Nulend J, Bacabac RG, Mullender MG. Mechanobiology of bone tissue. *Pathologie-biologie.* 2005;53(10):576-80.

## CHAPTER 5

### CONCLUSIONS

#### 5.1 Summary of Findings

The overall objectives of this work were to extend the understanding of biomechanical influences on musculoskeletal tissue injury models and repair implants. To accomplish this, an experimental biomechanical approach was taken to study (1) accelerated knee cartilage degeneration following joint destabilization and (2) mechanical characteristics of spine fusion implant designs influential to repair success. In summary, the novel methodologies were:

- (A) Development of a rabbit cyclic knee articulation platform to induce articular cartilage degeneration in an accelerated approach (**Chapter 2**).
- (B) Development of a mechanical testing platform compatible with high-resolution micro-computed tomography, which allowed image-based assessment of micro-scale strains in orthopedic implants under load (**Chapter 3, 4**).

The major findings related to the scientific objectives were:

1. *Ex vivo* cyclic knee articulation induces cartilage degeneration patterns in ACLT knees mimicking *in vivo* patterns of PTOA observed in rabbits (**Chapter 2**).

- a. Anterior drawer laxity increased with ACLT ( $4.07\pm 0.43\text{mm}$ ) compared with NL ( $0.76\pm 0.14\text{mm}$ ) and SH ( $0.86\pm 0.21\text{mm}$ ), demonstrating a mechanism for joint destabilization. Tibial anterior-posterior translation was increased in ACLT ( $0.68\pm 0.26\text{mm}$ ) compared to SH ( $0.33\pm 0.15\text{mm}$ ) during simulated gait.
  - b. India ink reflectance scores were diminished (indicative of degeneration) in the posterior regions of MFC (-63%) and LFC (-38%) in ACLT knees at 1000 cycles, compared with SH. India ink and 3-D histology demonstrated progressive increase in wear with loading cycles.
2. Spine fusion implants loaded in a physiologic range exhibit strains consistent with bone mechanobiological homeostasis (**Chapter 3**).
    - a. Cages exhibited increases in strut strain amplitude when loaded from 50N to 1000N or 2000N. At 2000N, 59-64% of struts exhibited strain amplitudes consistent with mechanobiologically-regulated bone homeostasis.
3. Spine fusion implants design and load amplitude alter the distribution of strains exhibited by implant struts and effective compressive modulus (**Chapter 4**).
    - a. Cages designed with thinner (0.75mm and 1.00mm, instead of 1.25mm diameter) struts resulted in higher percentages of struts in homeostasis and formation ranges under moderate (1000N) and strenuous (2000N) axial compressive loads.
    - b. The effective compressive modulus was dependent on strut diameter, with modulus decreasing from  $12.1\pm 2.3\text{GPa}$  (1.25mm) to  $9.2\pm 7.5\text{GPa}$  (1.00mm) and  $3.8\pm 0.6\text{GPa}$  (0.75mm).

- c. These findings suggest that future cage and orthopedic implant designs may be modulated to target desired mechanical strain regimes at physiological loads.

## 5.2 Discussion

The presented work focused on developing novel biomechanical platforms to advance the understanding of musculoskeletal diseases on two fronts: (1) expanding the understanding of a mechanically-driven mechanism for post-traumatic cartilage pathology, and (2) elucidating the mechanical responses of spine repair implants under physiological loads to inform current and future designs. These goals spanned across multiple facets of medicine, from understanding and replicating a disease process to assessing a therapeutic repair intervention.

In developing the *ex vivo* mechanical loading model for PTOA, a number of methodological advances were made. This work extended common engineering materials failure testing to the dynamic loading environment of the rabbit knee during articulation to achieve a mechanically-induced PTOA injury model. The loading apparatus was designed to replicate simplified rabbit knee articulation via dynamic feedback-controlled electromechanical tensioning of loading lines to simulate alternating contraction of antagonizing muscle groups (quadriceps, gastrocnemius). This continuous cyclic loading allowed for accelerated study of cartilage degeneration of ACLT vs SH in the timescale of hours, rather than weeks or months in the case of *in vivo* models.

The *ex vivo* loading model confers a number of advantages compared to traditional *in vivo* models for PTOA in the rabbit. The magnitude of gross degeneration at 1000 cycles (~30 minutes of loading time) was comparable to that of 4 weeks *in vivo* locomotive loading in the post-ACLT rabbit. Studies have demonstrated notable surface and histological cartilage damage as early 2 weeks, but more prominently at 4 and 8 weeks post-ACLT [1-3]. This equates to a

substantial study time and cost savings over *in vivo* rabbit models. The *ex vivo* approach also enables controlled and reproducible loading cycles, which can be adjusted to speed and load amplitudes for both muscle groups. By varying total cycle counts, the progression of cartilage degeneration may be studied as a surrogate for extended periods of *in vivo* study time.

As a simplified gait model, knee loading differed from physiological environment in a number of ways. Reduction of complex knee loading to the primary pair of muscles responsible for knee extension (quadriceps) and flexion (gastrocnemius) in the rabbit omits other muscles groups that contribute to other modes of knee motion and provide stability [4,5]. Passive stabilizing elements (ligaments, meniscus, synovial capsule) were retained intact. Similarly, ground reaction forces were not included in this model, which likely contribute to loading through the knee during rabbit gait. The loading pattern was also simplified as sequential ramp/relax cycles for the quadriceps and gastrocnemius, as the time course of load magnitudes through the hop cycle is not well understood for the rabbit [4]. Since this approach focused on mechanically-driven wear, the complex biological response leading to PTOA *in vivo* was not considered [6,7]. As the tissues were presumably not viable, chondrocyte and matrix metabolism mechanisms that may accelerate or protect cartilage were minimized, and synovial fluid lubricants were not replenished.

This novel *ex vivo* loading approach provides a platform for a variety of future studies. The spatiotemporal patterns and progression of cartilage damage may be elucidated to model those recognized in the human knee. Modulating the load amplitude, pattern, and cycle number may delineate responses to chronic vs impact overloading regimes. Therapeutic interventions to mitigate cartilage degeneration in this PTOA model may be assessed in a controlled *ex vivo* setting. This loading platform may also be expanded in the future to account for additional

muscle groups and ground reaction forces to more closely replicate the *in vivo* loading environment.

In order to achieve high sensitivity strain mapping of a loaded spine implant, a number of technological advancements were made. By combining high resolution 3-D imaging (micro-CT) with application of physiological loads to implants with an array of affixed fiducial markers, strain could be assessed for each individual truss, which would not be feasible with traditional instrumentation approaches. Specialized micro-CT compatible compressive loading devices with load monitoring were designed for non-destructive implant loading. Using developed 3-D image processing and analysis methods, high sensitivity strains ( $\sim 100 \mu\epsilon$ ) could be detected throughout an implant volume.

The scope of this work encompassed the assessment of primary strain responses to simplified physiological loading conditions. Loading conditions were approximated to be axial compression, consistent with the primary *in vivo* component in the spine [8,9]. However, the spine and associated bone-implant-bone complex exhibits complex loading conditions associated with multiple passive and active loading structures as well as complex interface geometry [10]. Whereas these were simplified to enable robust study of primary loading variables, the methodology may be refined in the future to address such complexities to further approximate the *in vivo* loading environment. Similarly, characterization was limited to linear axial deformation and strain for each truss strut, which is consistent with the simplified principles of a mechanical truss structure. Future studies may consider analyzing additional types of strain, such as bending, torsion, and shear. Static loading may be expanded to dynamic loading to further approximate the *in vivo* loading condition, especially as these methodologies may be applied to non-elastic materials, such as biological grafts or constructs.

This imaging under load approach to implant mechanical assessment can be expanded across other fields of medicine, particularly orthopedics. Orthopaedic implants have increasingly adapted structural and material designs to consider mechanical interactions with surrounding tissues and mechanobiological implications for repair [11-14]. As implant designs increase in complexity to address such goals, there will likely arise a need for experimental assessment of mechanical characteristics to validate theoretical numerical simulations. Future study of medical implants *in vitro* and *ex vivo* using image-based tracking combined with loading regimes may be warranted. Furthermore, extension to mechanical assessments *in vivo* may be useful as a metric for implantation success or for prediction of implant failure. Such methodologies may expand into regenerative medicine, such as with integrity monitoring of particle-laden implantable repair tissues or constructs.

In conclusion, these novel musculoskeletal mechanical loading platforms serve as scientific tools for the study of mechanisms of pathology and assessment of repair implants. This work helps enable the future understanding of disease models, as well as the development and improvement of therapeutic interventions.



### 5.3 References

1. Batiste DL, Kirkley A, Lavery S, Thain LM, Spouge AR, Gati JS, Foster PJ, Holdsworth DW. High-resolution MRI and micro-CT in an ex vivo rabbit anterior cruciate ligament transection model of osteoarthritis. *Osteoarthritis Cartilage*. 2004;12(8):614-26.
2. Batiste DL, Kirkley A, Lavery S, Thain LM, Spouge AR, Holdsworth DW. Ex vivo characterization of articular cartilage and bone lesions in a rabbit ACL transection model of osteoarthritis using MRI and micro-CT. *Osteoarthritis Cartilage* 2004; 12: 986-996.
3. Kajabi AW, Casula V, Ojanen S, Finnila MA, Herzog W, Saarakkala S, Korhonen RK, Nissi MJ, Nieminen MT. Multiparametric MR imaging reveals early cartilage degeneration at 2 and 8 weeks after ACL transection in a rabbit model. *J Orthop Res*. 2020.
4. Gushue D, Houck J, Lerner A. Rabbit knee joint biomechanics: Motion analysis and modeling of forces during hopping. *J Orthop Res* 2005; 23: 735-742.
5. Grover DM, Chen AA, Hazelwood SJ. Biomechanics of the rabbit knee and ankle: muscle, ligament, and joint contact force predictions. *J Biomech* 2007; 40: 2816-2821.
6. Anderson DD, Chubinskaya S, Guilak F, Martin JA, Oegema TR, Olson SA, Buckwalter JA. Post-traumatic osteoarthritis: Improved understanding and opportunities for early intervention. *J Orthop Res*. 2011;29(6):802-9.
7. Carbone A, Rodeo S. Review of current understanding of post-traumatic osteoarthritis resulting from sports injuries. *J Orthop Res* 2017; 35: 397-405.
8. Schultz AB, Andersson GB, Haderspeck K, Ortengren R, Nordin M, Bjork R. Analysis and measurement of lumbar trunk loads in tasks involving bends and twists. *J Biomech*. 1982;15(9):669-75.
9. Nachemson A. Towards a better understanding of low-back pain: a review of the mechanics of the lumbar disc. *Rheumatol Rehabil*. 1975;14(3):129-43.
10. Dolan P, Adams MA. Recent advances in lumbar spinal mechanics and their significance for modelling. *Clin Biomech* 2001;16:S8-S16.
11. Cowin SC, Hegedus DM. Bone remodeling I: A theory of adaptive elasticity. *J Elasticity*. 1976;6:313-25.
12. Turner CH. Three rules for bone adaptation to a mechanical stimuli. *Bone*. 1998;23:399-407.

13. Frost HM. Bone's mechanostat: a 2003 update. *Anat Rec A*. 2003;275(2):1081-101.
14. Reid JJ, Johnson JS, Wang JC. Challenges to bone formation in spinal fusion. *J Biomech*. 2011;44(2):213-20.